Lecture Notes in Physics 875

Christian Beck *Editor*

Clusters in Nuclei, Volume 3

Springer

Chapter 6
Clusterization in Ternary Fission

D.V. Kamanin and Y.V. Pyatkov

6.1 Searching for New Ternary Decays—Background and Motivation

The present paper is devoted to the observation of a new kind of ternary decay of low-excited heavy nuclei. This decay mode has been called by us "collinear cluster tri-partition" (CCT) in view of the observed features of the effect, that the decay partners fly apart almost collinearly and at least one of them has magic nucleon composition. CCT is observed together with conventional binary and ternary fission. It could be one of the rare fission modes, but at the moment this assumption is not an established fact. For instance, many years have passed between the experimental discovery of the heavy ion radioactivity and working out of a recognized theory of the process.

Nuclear fission, a process where a heavy nucleus decays into two fragments of intermediate mass (e.g. Ba + Kr) has been identified by Hahn and Strassmann in 1938. It was discovered by chemical analysis while irradiating natural Uranium with thermal neutrons [1]. Shortly afterwards Petrzhak and Flerov [2] observed spontaneous fission of the ^{238}U isotope. The energy release in the fission process was immediately calculated by all leading physicists at that time to be very large, typically 200–205 MeV (e.g. Meitner and Frisch [3]). The large value is due to the larger binding energy per nucleon (E_B/N) in the mass range around mass $A = 54$ (iron, $E_B/N = 8.2$ MeV), as compared to the value at the end of the periodic table, ($E_B/N = 7.2$ MeV). This fact could have been noticed four years before

D.V. Kamanin (✉) · Y.V. Pyatkov
Flerov Laboratory of Nuclear Reactions, Joint Institute for Nuclear Research, Joliot-Curie 6, Dubna 141980, Moscow Region, Russia
e-mail: kamanin@jinr.ru

Y.V. Pyatkov
National Nuclear Research University "MEPHI", Kashirskoe shosse 31, Moscow 115409, Russia
e-mail: yvp_nov@mail.ru

C. Beck (ed.), *Clusters in Nuclei, Volume 3*, Lecture Notes in Physics 875,
DOI 10.1007/978-3-319-01077-9_6,

these discoveries, because of the existence of the liquid drop model and the nuclear mass formula of Bethe and Weizsäcker [4]. However, the large collective motion through a large deformation (today called super-deformation) was considered to be unlikely.

Fission of heavy low-excited nuclei into three fragments of comparable masses, so called "true ternary fission", has been intensively investigated soon after the discovery of fission. Swiatecki [5] has shown within the framework of the liquid-drop model (LDM) that fission into three heavy fragments is energetically more favourable than binary fission for all nuclei with fissility parameters $30.5 < Z^2/A < 43.3$. On the basis of a modified liquid-drop model that takes into account the finite range of the nuclear forces the macroscopic potential energy maps for symmetric systems of interest were calculated [6]. These maps demonstrate many important features of the potential energy landscape, including the heights and locations of the binary, ternary, and quaternary fission saddle points. In 1963 Strutinsky [7] has calculated the equilibrium shapes of the fissioning nucleus and has shown, that along with the ordinary configuration with one neck, there is the possibility of more complicated elongated configurations with two and even three necks, at the same time it was stressed, that such configurations are much less probable. Later Diehl and Greiner [8, 9] have shown a preference for prolate over oblate saddle-point shapes for the fission of a nucleus into three fragments of similar size. Such pre-scission configurations could lead to almost collinear separation of the decay partners, at least in a sequential fission process. Actually the Coulomb interaction in the total potential energy is the smallest for linear arrangements of the three fragments. Ternary potential barriers as a function of the distance between the mass centers of the fragments were calculated in Ref. [10]. In the ternary fission path, the isomeric states corresponding to elongated and compact shapes were predicted for heavy systems. Investigating ternary fission of the system $^{238}U + ^{238}U$ the authors of [11] came to conclusion that binary fission is much more probable than ternary fission even among very heavy compound nuclei. The reasons for this are that the LDM potential for ternary fission turns out to be higher than that for binary fission at large deformations and that the formation and rupture of necks for binary fission occur much earlier in the fission process than for ternary fission. However, it was emphasized that very strong shell effects might also lead to earlier ternary neck formation during fission. Results demonstrating a decisive role of shell effects in the formation of the multi-body chain-like nuclear molecules were obtained by Poenaru et al. [12]. We want to refer as well on very recent theoretical articles, devoted to unusual ternary decays of heavy nuclei including CCT [13–16]. The authors analyze the potential energy of different pre-scission configurations leading to ternary decays, and the kinetic energies of the CCT partners [17] are calculated for a sequential decay process. These results, being strongly model dependent can be considered as only the first step in the description of the CCT process.

On the experimental side there have been multiple attempts to find the true ternary fission in low energy fission by means of counting techniques and in radiochemical studies. The schemes of the spectrometric experiments were based on the assumption of comparable angles between all three fragments emitted [18, 19].

Masses of the fragments were calculated in this case based on experimental values of the energies and angles. Contradictory results have been obtained; these were treated as showing the absence of fission fragments in the vicinity of mass fifty both in binary and ternary fission [20]. The latest attempt to find very specific ternary decay mode similar to the CCT in ^{252}Cf nucleus is reported in series of works [21–24]. Spontaneous cold ternary decay showing the nuclei of ^{96}Sr, ^{146}Ba and ^{10}Be in the exit channel was searched for. The experiment was carried out at the Gammasphere and gamma-gamma coincidences were analyzed. At the first stage of the work the authors came to conclusion that ^{10}Be nucleus stays at rest after fission but later this conclusion was not confirmed. At the same time almost collinear ternary decays of excited heavy nuclear systems were known from the experiments in Refs. [25, 26] at the early stage of our work.

In the highly excited nuclear systems produced by the nucleus-nucleus collisions in the intermediate energy domain (20–100 MeV/u) the binary fission remains an important exit channel. Nevertheless, the ternary, quaternary, quinary ... decays have been observed [27, 28]. The interpretation of this multi-fragment production is still elusive, but all the models put forward so far (dynamically induced density fluctuations, expansion of an initially compressed source, statistical decay and so on) are valid exclusively for hot nuclear matter at the excitations far beyond the region where shell effects manifest themselves.

As was mentioned above, at least one of the CCT products has magic nucleon composition. Shell effects give rise also to two well-known binary decay modes: namely, cluster radioactivity and cold fission. Evident and deep link between all three processes demands to remind briefly the main features of these binary decays.

Cluster radioactivity as a rare spontaneous decay mode of heavy nuclei has been intensively studied in recent years. In this type of radioactivity any emitted nuclear species with masses heavier than $A = 4$ (α-particles) and lighter than $A \approx 60$ (fission fragments) are called "clusters". The heavy fragments are grouped in the vicinity of the double magic ^{208}Pb, and this allows speaking about the known domain of cluster decay as "lead radioactivity". This type of radioactivity is far from being unique. Many other combinations of daughter nuclei are allowed energetically to be emitted; they include the formation of the products of comparable masses. This process is known as cold fission. However, cluster radioactivity is a very rare process: the observed partial life times lie in the interval 10^{11}–10^{27} s. This corresponds to a branching ratio relative to 10^{-10}–10^{-17} for those α-decays.

In all known cases, except for one, the products of cluster radioactivity are formed in their ground states. From this point of view cluster radioactivity is much closer to alpha-decay than to spontaneous fission, the process in which the both fragments are deformed and strongly excited. For this reason correct comparison of both processes can be done only if cold fission is meant because here the fragments are formed in their ground or low-lying excited states. However, cold spontaneous fission itself is studied even worse than cluster radioactivity. The question of what is the mechanism of cluster radioactivity and whether it resembles either α-decay or fission was widely discussed.

The authors of [29] made a survey of mass distributions of cold decays for a series of nuclei and drew some conclusions. Cold decays are distributed over the whole available range of masses. The phenomenon known today as "cluster radioactivity" is only a particular case of their more general family. It is not distinguished neither by the nature of its origin, nor by its probability in comparison with the other modes. One can speak about "lead", "tin" and "calcium" activities depending on the vicinity of Z- and N-values to the corresponding magic numbers. The most widespread activity is the "tin" one due to the fact that the ratio 82/50 is close to the average N/Z ratio of the decaying parent nuclei (this provides on the average the maximum Q-value). "Tin" activity drifts from very asymmetric one in the parent mass region $A \sim 150$ to symmetric fission for ^{264}Fm. Another source of enhancement of the decay probability is the formation of fragments having prolate static deformations. Orientation of the big axis along the direction of movement results in lowering of Coulomb barrier and diminishing the path under it. As a result, the authors conclude that one cannot distinguish between cold fission and different types of cluster radioactivity. However, the dynamics of fragment formation in different parts of mass spectra can be different. Alpha-radioactivity and fission usually are described by completely different formalism reflecting a different physical picture of what happens, and these extremes are applied to the description of cluster radioactivity.

Alpha-decay is considered to be a non-adiabatic process. It means a sudden formation of a cluster inside the mother nucleus which then makes attempts to penetrate the barrier. The fission-like process, on the contrary, is described as an adiabatic one. It includes the pre-scission phase where the matter flow takes place and fragments are overlapping. Their final formation happens only after the system goes through a sequence of geometrical shapes whose parametrization is a part of the adopted theoretical approach. The existing data and theoretical calculations indicate that cluster (at least "lead") radioactivity and cold fission have different mechanisms, probable non-adiabatic and adiabatic correspondingly. The transition between both mechanisms takes place at the fragment masses in the vicinity $A = 35$.

We would like to emphasize, that at the early stage of our work the process of "true ternary fission" (fission of the nucleus into three fragments of comparable masses) was considered to be undiscovered for low excited heavy nuclei [30]. Another possible prototype—three body cluster radioactivity—was also unknown. The most closest process to the CCT phenomenon, at least cinematically, is the so called "polar emission" [31], but only very light ions (up to isotopes of Be) have been observed so far. In the analysis of the experiments devoted to the "polar emission", we came to the conclusion that typical CCT fragments could not be detected in the cited works [32]. In fact, dE-E telescopes (energy-loss, energy) were used to stop the fission fragments (FFs) in the dE-detector located on the path of the light charged particles (LCP) flying in the same direction (polar LCP). At the same time this detector must be thin enough to be transparent for the LCP under study. The thickness of the dE-detectors, chosen as a compromise, puts a boundary for the mass/charge of the LCP, which could be detected.

Bearing in mind both theoretical and experimental results mentioned above, we came to the conclusion, that collinear tri-partition of low-excited heavy nuclear systems would be a promising field of research. In our first experiments dedicated to this problem [33, 34] some indications of such processes were already observed. At least one of the decay products detected was a magic nucleus. By analogy with known cluster decay (or lead radioactivity), the process has been called "collinear cluster tri-partition" (CCT).

6.2 Comparative Study of the CCT in ^{252}Cf (sf) and ^{235}U(n_{th}, f) Reaction

In the present section we describe the results of two different experiments devoted to the search for collinear tri-partition of heavy nuclei. In these experiments binary coincidences with two detector systems placed at relative angles of 180° are measured, see Figs. 6.1 and 6.2. Among all known detection methods to measure the masses of nuclear reaction products, the TOF-E (time-of-flight *vs.* energy) method is the only one which uniquely allows the study of multi-body decays. In this method both, the fragment velocities V obtained by means of TOF, and the energy E, are measured for each detected fragment individually. The fragment mass M_{TE} is calculated simply using the equation $M_{TE} = 2E/V^2$. For a three-body decay six variables determine the kinematics (i.e., 3 masses and 3 velocity vectors). Adding momentum conservation reduces the number of independent variables to four. In our experiments two masses and two velocities are determined for two fragments observed at a relative angle of 180°. Thus all the results presented below are obtained within the framework of the "missing-mass" approach. With the two-arm spectrometers binary coincidences have been measured, with a special mechanism, which blocks the registration of a third fragment, as explained above and in Fig. 6.1. This means that only two fragments were actually detected in each fission event and their total mass, the sum M_s will serve as a sign of a multi-body decay if it is significantly smaller than the mass of the initial system.

6.2.1 Experiment Ex1

In the first experiment (Ex1, Fig. 6.1), performed at the FOBOS [35] setup in the Flerov Laboratory of Nuclear Reactions (FLNR) of the Joint Institute for Nuclear Research (JINR) in Dubna, about 13×10^6 coincident binary fission events of ^{252}Cf were collected. The TOF of the fragment was measured over a flight path of 50 cm between the "start" detector (label (3) in Fig. 6.1), which is based on micro-channel plates (MCP) placed next to the ^{252}Cf-source and the "stop" one represented by position sensitive avalanche counters (PSAC, 4). The source activity was 370 fissions/s, it was deposited on a Al_2O_3 backing of 50 μg/cm^2 thickness and 18 mm

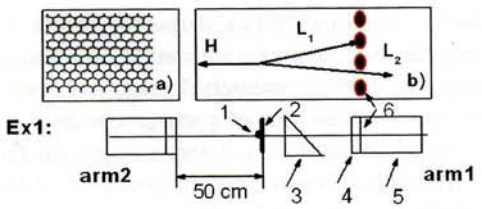

Fig. 6.1 Scheme of (Ex1) for coincidence measurements of two fragments of the fission decay of ^{252}Cf. This experiment has been performed at the FOBOS setup [35]. Here: *1*—Cf source, *2*—source backing, *3*—micro-channel plate (MCP) based timing "start" detector, *4*—position sensitive avalanche counter (PSAC) as "stop" detector, *5*—ionization chamber (BIC) with the supporting mesh, *6*—mesh of the entrance window. The front view of the mesh is shown in the insert (**a**), an enlarged mesh section is presented in the insert (**b**). After passage of the two fragments through the source backing, two light fragments L_1 and L_2, are obtained with a small angle divergence due to multiple scattering. In (**b**) we show that one of the fragments (L_1) can be lost hitting the metal structure of the mesh, while the fragment L_2 reaches the detectors of the arm 1. The source backing (2) exists only on one side and causes the mentioned angular dispersion in the direction towards the right arm 1

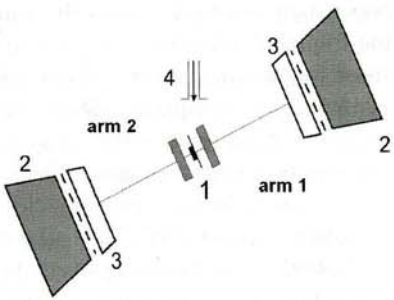

Fig. 6.2 Scheme (Ex2) of the mini-FOBOS spectrometer which includes a "start" avalanche counter with an internal target (*1*), Bragg ionization chambers (BIC) (*2*) and "stop" position-sensitive avalanche counters (PSAC) (*3*). The target is irradiated by a collimated beam of thermal neutrons (*4*)

in diameter—(1). Through the measurements of the position of the fragments in the PSAC's, this information provided also the fragment's emission angle with a precision of 1^0. The energies of those coincident fragments which passed through the PSACs were measured in the Bragg ionization chambers (BIC, label 5 in Fig. 6.1). The entrance windows of the large BIC are made of 1 μm thick aluminized Mylar, with a diameter of 385 mm. To withstand the pressure of the counting gas, the delicate window foil has to be supported by a two-fold structure—a concentric heavy carrier of a transparency of 94 % and an adjacent etched Ni-mesh having a cell dimension of 2.7 mm in diameter and 0.9 mm bulkhead in between the open pores. The thickness of the mesh is about 1 mm. The geometrical structure of the mesh is hexagonal, its front view is shown in the insert (a) of Fig. 6.1, a mesh section is presented in the insert (b). The mesh reduces the total transparency to 75 %. This mesh is a very important peculiarity of the present experiments as explained below (see Fig. 6.1).

6.2.2 Experiment Ex2

For a better understanding of the unusual decay channel in ^{252}Cf (sf) we planned to investigate different fissile systems at different excitation energies up to the threshold of the survival of nuclear shells. One of the reactions we had chosen in an additional experiment was fission induced by thermal neutrons in ^{235}U(n_{th}, f).

The experiment (Ex2) was performed with a beam of thermal neutrons of the IBR-2 reactor in the Frank Laboratory of Neutron Physics of the JINR with the help of the double-armed TOF-E mode of the mini-FOBOS [36] spectrometer. The overall statistics processed in this experiment was about 2×10^6 fission events. The scheme of the setup is shown in Fig. 6.2. The spectrometer is also based on FOBOS detector modules. The start detector is a symmetrical avalanche counter with internal target. The active layer of the target material was prepared by evaporation of 100 μg/cm^2 of ^{235}U on an Al_2O_3 backing of 50 μg/cm^2 thickness. In this case along with measuring the fission fragment (FF) time-of-flight (TOF) and their energies (E), two more parameters being sensitive to the nuclear charge are added. The drift time of the track formed after stopping of a fragment in the gas volume of the BIC is known to be linked with the fragment's nuclear charge [37]. The corresponding parameter was measured as the time difference between the PSAC signal and the signal from the Frisch grid of the BIC. Special calibration procedures have been worked out for the FF nuclear charge determination [38]. According to the tests carried out before, the charge resolution does not exceed 3.8 units (FWHM) for the FF from the light mass peak, while the mean values for each fixed charge are correctly determined.

The second independent variable, which is also sensitive to the nuclear charge, is the specific energy loss of the FF in the gas volume of the PSAC [35]. This parameter proved to be very useful also for the selection of the CCT events.

In both experiments similar procedures for the TOF-E calibration and the calculation of the M_{TE} masses were used. In brief, the mass spectrum of binary decays, which depends on the measured variables and parameters to be determined, was fitted to the known mass spectrum of ^{252}Cf fission [39]. The data presented in Fig. 6.3 were obtained in the following way. For each fixed experimental M_{TT}(TOF, TOF) mass a corresponding mean value of M_{TE} was obtained. $M_{TT}{}^{(1)}$ (primary, i.e., the fragment mass before neutron emission) was calculated as $M^{(1)}{}_{TT} = M_c/(1 + V_1/V_2)$, where M_c—the mass of the fissioning system, $V_{1,2}$—velocities of the coincident fragments (indices correspond to the numbers of the spectrometer arms). The values $\langle M_{TE} \rangle$ are compared with their values expected for, i.e., M_{TT}—$\nu(M_{TT})$, where $\nu(M_{TT})$—mean number of neutrons emitted from the fragment of the mass M_{TT}, taken from Ref. [40]. Thus, Fig. 6.3 demonstrates the absence of shifts (essential nonlinearity) in the calibration of the M_{TE} masses. This point is very important for correct treatment of the data, especially for the mass characteristics and the peculiarities discussed below such as peaks and ridges in the spectra and distributions, respectively.

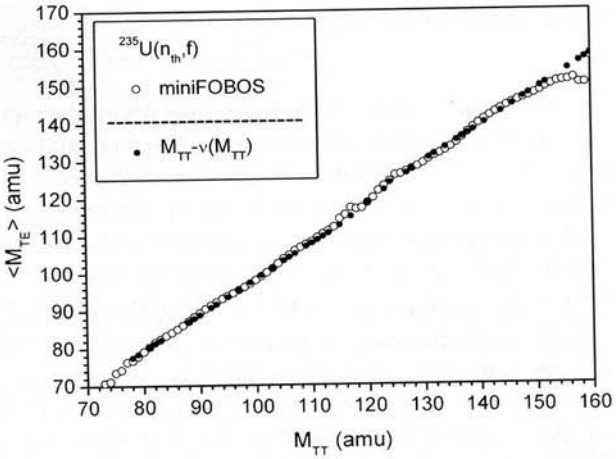

Fig. 6.3 Correlation of the mean values of the experimental mass $\langle M_{TE} \rangle$ (post-neutron emission) *vs.* mass, M_{TT}, obtained in the present TOF-TOF analysis. The shift due to neutron emission $\nu(M_{TT})$ [40] has been taken into account

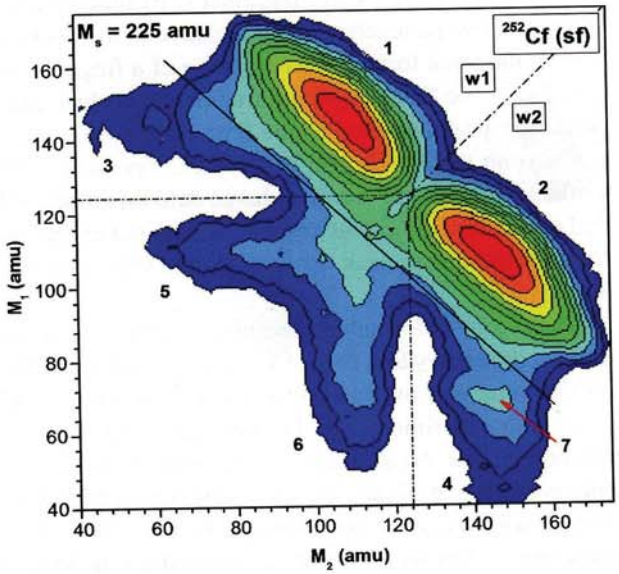

Fig. 6.4 Contour maps (in logarithmic scale, the steps between colors are approximately a factor 2.5) of the mass-mass distribution of the collinear fragments, detected in coincidence in the two opposite arms of the FOBOS spectrometer in Ex1. The additional bump (7) in arm1 is indicated by an *arrow*. Two large windows *w*1 and *w*2 are used in the later analysis (Sect. 6.3). See text for details

6.2.3 *Results of Experiment Ex1, ^{252}Cf (sf)*

Figure 6.4 shows in a logarithmic scale the two-dimensional distribution (M_2–M_1) of the two registered masses of the coincident fragments in the experiment (Ex1). In this FOBOS setup M_1 is defined as the fragment mass derived from the arm facing to the additional dispersive (scattering) materials. Only collinear fission events with a relative angle of $180 \pm 2°$ were selected, which corresponds to the typical angular spread for conventional binary fission fragments.

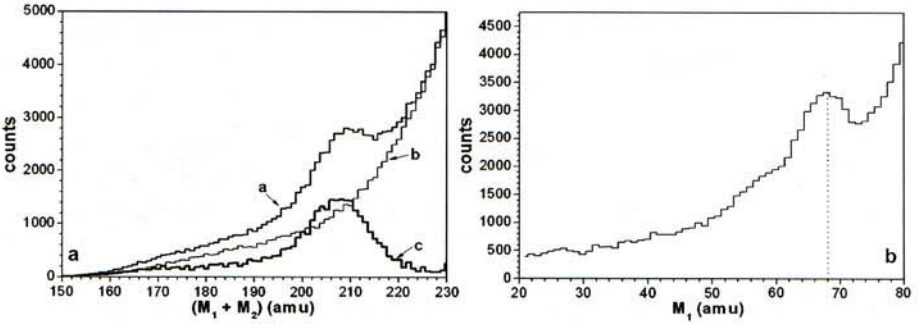

Fig. 6.5 The bump "7" from (Ex1) in Fig. 6.4 is analyzed. In (**a**) the spectra of the summed masses M_s for the "tails" (4 and 3) shown as spectrum *a* and *b*, respectively, are compared. The result of the subtraction of spectrum *b* from spectrum *a* (difference spectrum) is marked as *c*. On the *right side*, part (**b**), the projection of the bump onto the M_1 axis is shown

The "tails" in the mass distributions marked 3–6 in Fig. 6.4 extending from the regions (1) and (2) which are used to mark conventional binary fission, are mainly due to the scattering of fragments on both the foils and on the grid edges of the "stop" avalanche counters and the ionization chambers. Once again we emphasize the small but important asymmetry in the experimental arrangement between the two arms, which consists in location of both the thin source backing (50 $\mu g/cm^2$ of Al_2O_3) at the "rear side" of the target and the "start" detector foil only in arm 1 (Fig. 6.4). An astonishing difference in the counting rates and in the shapes of the "tails" (3) and (4) attracts attention. In the case shown in Fig. 6.4 there is a distinct "additional" bump, marked (7), on top of the latter "tail" (4). The bump is located in the region corresponding to a large "missing" mass. In Fig. 6.4 the line for the measured total mass $M_s = M_1 + M_2 = 225$ amu is shown as a border line separating these interesting events from normal binary fission. Statistical significance of the events in the structure (7) can be deduced from Fig. 6.5, where the spectra of total (summed) masses M_s for the "tails" (4) and (3) are compared. The yield of the events in the difference spectrum *c* is $(4.7 \pm 0.2) \times 10^{-3}$ relative to the total number of events in the distribution shown in Fig. 6.4. It is only a lower limit of the yield due to the reasons discussed below. In order to explain the differences in the "tails" (4) and (3) mentioned above (see also Fig. 6.7), the following scenario is proposed, and the corresponding geometry has been shown in Fig. 6.1 (insert b). We assume that in ternary fission three fragments are emitted collinearly due to two sequential binary decays. Two of the fragments are emitted in one direction but become separated in their velocity vectors with a small angle difference of $\sim 1°$ after passing the scattering media, due to multiple scattering [41]. These media are the backing of the source and the foil of the start detector both located only on the side of tail (4). For instance, for a ^{70}Ni fragment with the energy 70 MeV the mean angle of multiple scattering in the backing is equal to 0.64° while the tail of the angular distribution extends up to 2°. As a result two fragments continue to fly in the same direction with a small angle divergence.

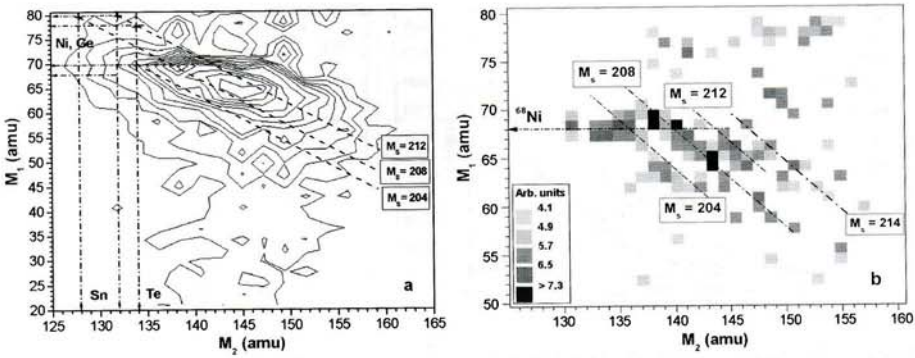

Fig. 6.6 *Left side*, (**a**): The figure depicts as a $2D$-contour map (M_1 *vs* M_2) the difference between the "tails" (4) and (3), for the events measured in Ex1, with the system shown in Fig. 6.1. *Dashed lines* tilted by 45° with respect to the M_2 axis correspond to a fixed total mass of the two detected fragments $M_s = M_1 + M_2 = \text{const}$. Part (**b**): the same as in (**a**), however, passed through a second derivative filter which emphasizes local peaks in each section of $M_s = \text{const}$. The ridges correspond to different values of M_s (204, 208, 212 and possibly 214 amu). The *arrows* in the figures mark positions of magic isotopes on the mass axis. Their role in the CCT process is discussed in the text

Thus, if both fragments pass on and enter into the BIC, we register a signal corresponding to the sum of the energies of these two fragments. In this case the event will be treated as binary fission with the usual parameters. In the other cases only the proper energy (mass) of one of the light fragments is measured, because the second one is stopped (lost) in the supporting grid of the ionization chamber. Just the absence of a similar grid is likely the reason why the authors of the work in Ref. [42] have failed to observe collinear ternary decays of ^{252}Cf (sf) using the time-of-flight method.

For a more detailed analysis of the bump we have constructed the contour map of the two-dimensional mass-mass distribution obtained by subtraction of the "tail" (3) from the "tail" (4) (Fig. 6.6(a)). No additional normalization was used.

This distribution is almost free from experimental background originating from scattered fragments of ordinary binary fission. Some features of this $2D$ plot can be further emphasized by procesing of the distribution with a second derivative filter (Fig. 6.6(b)), such method which is typically used in the search for peaks in gamma spectra, and it is explained in more detail in Refs. [43, 44]. The vertical scale (reversed values of second derivative) represented by the squares is defined in the insert to this figure. The maxima of the peaks extend over certain linear regions of $M_2 = \text{const}$, which are found predominantly as discrete diagonal lines, marked in Fig. 6.6(b). Note that they correspond to the total masses $M_s = \text{const}$ with values of 204, 208, 212 and perhaps 214 amu, respectively. To show the positions of the tilted ridges on the map of the bump they are marked by the dashed lines in Fig. 6.6(a). As can be deduced from the figure, the ridges go through crossing points corresponding to different combinations of two fragments with magic nucleon numbers (marked by the dot-dashed arrows). These marked points could be related to mass values with magic subsystems, well-known from binary fission [45, 46] as follows (correspond-

ing rounded Q values for ternary decays are marked in braces): $204 \rightarrow {}^{70}\mathrm{Ni}$ ($Z = 28$) $+ {}^{134}\mathrm{Te}\{241\ \mathrm{MeV}\}$ or ${}^{72}\mathrm{Ni} + {}^{132}\mathrm{Sn}$ ($Z = 50$) $\{251\ \mathrm{MeV}\}$, $208 \rightarrow {}^{80}\mathrm{Ge} + {}^{128}\mathrm{Sn}$ $\{261\ \mathrm{MeV}\}$ and for $212 \rightarrow {}^{80}\mathrm{Ge} + {}^{132}\mathrm{Sn}$ $\{257\ \mathrm{MeV}\}$, ${}^{78}\mathrm{Ni} + {}^{134}\mathrm{Te}$ $\{228\ \mathrm{MeV}\}$ or ${}^{68}\mathrm{Ni} + {}^{144}\mathrm{Ba}$ $\{217\ \mathrm{MeV}\}$ and for $M_s = 214 \rightarrow {}^{82}\mathrm{Ge} + {}^{132}\mathrm{Sn}$ $\{226\ \mathrm{MeV}\}$. It should be reminded that the Q value that corresponds to the most probable binary partition of ${}^{252}\mathrm{Cf}$ is about 216 MeV.

Of course, at the moment this interpretation of the tilted ridges is only a hypothesis to be confirmed by the other results shown below.

The ridges discussed are crossed as well by the horizontal ridge (seen via bunching of contour lines in Fig. 6.6(a)). The projection of the bump onto the M_1 axis (Fig. 6.5(b)) confirms this conclusion. The effect is linked with the isotopes of ${}^{68,70}\mathrm{Ni}$, which are also magic [46]. Due to this fact we call the bump under discussion as "Ni"-bump.

6.2.4 *Results of Experiment Ex2,* ${}^{235}\mathrm{U}(n_{th}, f)$

The mere fact of the existence of the bump in the total mass as discussed above, as well as the presence of its internal structure was confirmed in an experiment (Ex2) devoted to the ${}^{235}\mathrm{U}(n_{th}, f)$ [47], in which nuclear charges were measured in addition.

A bump similar to that marked by an arrow in Fig. 6.4 is again well pronounced as shown in Fig. 6.7(a). The yield of the events in the bump is $(5.1 \pm 0.4) \times 10^{-3}$ relative to the total number of fission events detected. As in the previous case the bump is observed only in one spectrometer arm (marked by number 1) facing to the target backing. The projections of the bump onto the M_1 axis for both reactions are compared in Fig. 6.7(b). The pronounced peaks in both cases are centered at the masses (68–70) amu, associated with the magic isotopes of Ni. Projections onto the $M_s = \mathrm{const}$ direction are shown in Fig. 6.7(c). Although the total masses of the corresponding two fissioning systems differ by 16 amu the projections of the bump onto this direction are shifted no greater than 6 amu. Such shift of the top yield in the frame of the wide peak could be assigned to the different population of the fission modes based on magic pairs of Sn/Ge or Sn/Ni isotopes in Cf and U* nuclei.

We show the comparison of the spectra of nuclear charges of the measured FF in the two opposite spectrometer arms in Fig. 6.8. The result for the measured charges confirms the previous finding with the mass distributions, namely, the existence of an "additional" bump in the arm with the scattering media. It confirms the hypothesis that the upper boundary of the "additional" bump (Fig. 6.7(a), and (b)) is actually connected with Ni isotopes.

As was mentioned above, the presence of the tilted ridges $M_s = \mathrm{const}$ for the ${}^{252}\mathrm{Cf}$ nucleus was revealed using a special mathematical process for the FF mass-mass distribution. This fact has been confirmed independently for the ${}^{236}\mathrm{U}^*$ system by using selection with an additional parameter, namely, the specific energy losses dE of the FF in the "stop" avalanche counter.

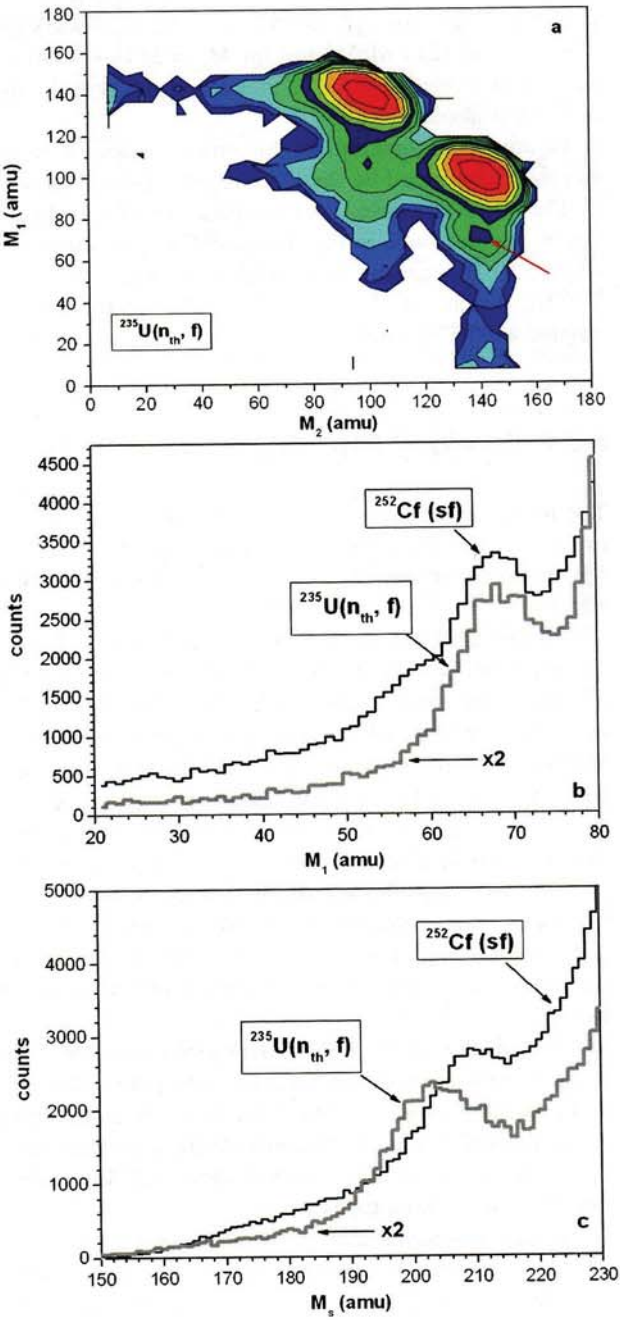

Fig. 6.7 (**a**) FF mass-mass distribution (logarithmic scale) obtained for the $^{235}\mathrm{U}(n_{th}, f)$ reaction. (**b**) Projections of the bump onto the M_1 axis for comparison of the reactions discussed here. (**c**) Projections of the bump onto the direction $M_s = M_2 + M_1 = \text{const}$

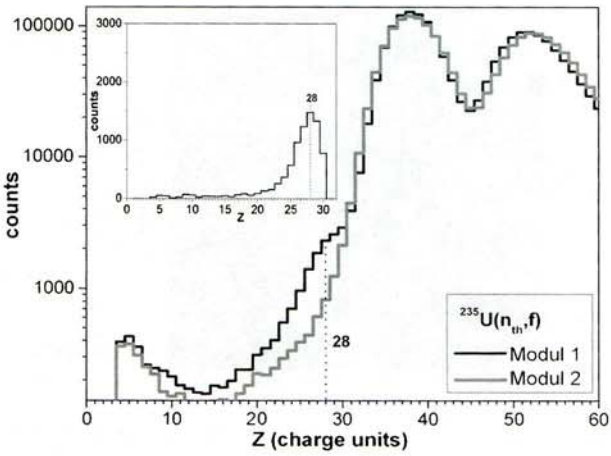

Fig. 6.8 Nuclear charge spectra from the FF from the reaction $^{235}\mathrm{U}(n_{th}, f)$, the FF are detected in the two opposite spectrometer arms. A difference in the yields (bump) presented in the *upper panel* in a linear scale is visible for the charges around $Z = 28$ (isotopes of Ni)

In Fig. 6.9 we show the mass-mass distribution of those FF, selected by this additional parameter, of an increased energy loss in comparison to FF from the light mass peak of normal binary fission. In this way we can select the events when a "fork" of two fragments of a ternary decay fly into the same first spectrometer arm, i.e., where the bump is observed. Total energy losses of these two fragments in the same counter have values, which are higher compared with the dE values for ordinary light fragments. It should be stressed that in this case the experimental variables used for gating (specific energy losses *vs.* velocity) are not distorted due to scattering on the entrance grid of the BIC, being the main source of the background events.

In the bump region a tilted valley structure with reduced event density is clearly seen indicating the presence of ridges with specific total masses, $M_s = \text{const}$ (Fig. 6.9(a)). It is marked by the tilted arrow. A projection of the bump onto this direction is shown in Fig. 6.9(b), the left bracket in the spectrum shows the mass region of potential location of pairs of magic isotopes $^{128,132}\mathrm{Sn}/^{68,70,72}\mathrm{Ni}$. Similarly the right bracket corresponds to pairs $^{128,132}\mathrm{Sn}/^{80,82}\mathrm{Ge}$. At least two peaks centered at the partitions marked in the figure (70/132 and 80/128 amu) are statistically significant. Actually, a parabolic (structureless) fit shown by the dot-dash line gives $\chi^2/f = 2.1$ (chi-square per degree of freedom), while a least squares approximation by the cubic spline (dot line) shows $\chi^2/f = 1.04$.

A peak centered at 68 amu comes out in the projection of the bump onto the M_1 axis in Fig. 6.9(c). Further as can be inferred from Fig. 6.9(a) the heavy fragments involved in the bump are bounded by the mass numbers in the region 128–144 associated with magic nuclei of $^{128}\mathrm{Sn}$ and $^{144}\mathrm{Ba}$. This conclusion is confirmed by the projection of the bump onto the corresponding axis (Fig. 6.9(d)), where the boundaries for Sn and Ba are shown. It should be noted that the internal structure of the bump seen in Fig. 6.9(a) is reproduced as well if the selection is made using a gate based on the drift time [48].

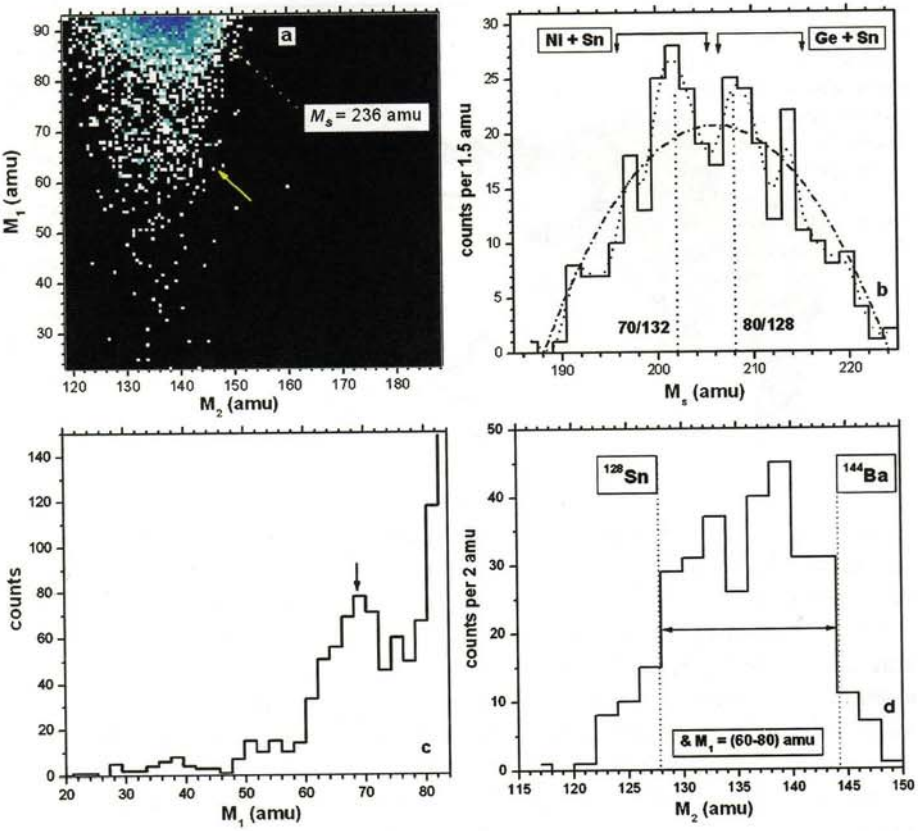

Fig. 6.9 (**a**) Mass-mass distribution of the fission events from the reaction $^{235}\mathrm{U}(n_{th}, f)$ selected by the additional gate on the velocity-energy-loss, the V–dE matrix; (**b**) Projection onto $M_1 + M_2 = \text{const}$ direction. Parabolic and spline least squares fits are shown by *dash-dot* and *dot lines*, respectively. (**c**) Projection of the distribution onto M_1 axis; and (**d**) Projection onto the M_2 axis for the events from the range $M_1 = (60\text{–}80)$ amu. See text for details

6.2.5 *Summary and Conclusions*

The present section has been devoted to the observation of a new multi-body decay channel called by us "collinear cluster tri-partition" (CCT). We observe in the mass-mass distributions ($2D$) the bump linked with large missing masses in the FF mass-mass distribution for cases, where the fragments passes through a dispersive medium providing an angular divergence between the two CCT partners flying towards the same spectrometer arm. The second principal feature of the spectrometer to be stressed is the presence of the blocking structure (grid or mesh) at the entrance to the BIC. Only the sequential action of these two technical details, namely angular struggling and blocking allows the detection of a CCT event, in the frame of the missing mass method. Earlier studies of spontaneous fission of ^{252}Cf in the

series of our experiments performed at different time-of-flight and energy spectrometers [49] gave the same observation when both masses of the coincident fragments were identified in the frame of the velocity-energy (V-E) method. Bearing in mind, that potentially scattering of fragments at the entrance to the E-detector could imitate these effects, we have used another approach with different experimental observables [50], which is methodically independent from FF masses investigated. Such approach was realized in the other experiment Ex2 discussed in the present paper.

We have shown in Ex2 (Fig. 6.9), that the selection of the fission events using V-dE (velocity-specific energy losses), confirmed not only the presence of the bump in the FF mass-mass distributions from the ^{235}U($n_{th,f}$) reaction, but also confirmed its internal structure. In particular an effective cleaning of the bump region from the background in this case, allowed us to observe directly the tilted ridges (and, respectively, the valleys in between). These again were found to correspond to total masses of pairs of magic clusters, namely, (Ni/Sn) or (Ge/Sn). The ridges under discussion are actually linked with pairs of magic clusters, they are the same for the two fissioning systems, namely, in ^{252}Cf and in ^{236}U*. Although these systems differ by 16 mass units, the position of the ridges stayed unchanged. In addition to the dE variable being absolutely independent from experimental mass values, an estimation of the nuclear charge (Z) via the drift time in the ionization chambers corresponds as well with the experimental fragment mass [38]. Thus the correct position of the bump in the nuclear charge of the fragments (projection on the Z axis in Fig. 6.8), gives clear arguments for the correctness of our assumption on the origin of the bump.

Experimental results suggesting the existence of a new decay mode, the collinear cluster tri-partition (CCT) decay channel, have been obtained [47, 51]. This decay mode manifests itself through a particular bump corresponding to a specific missing mass in the FF mass-mass distributions. One of the decay modes which contribute to the bump can be treated as a new type of cluster decay as compared to the well known heavy ion or lead radioactivity. Key features of both them are summed up in Fig. 6.10. The relatively high CCT yield can be understood if one assumes collective motion through hyper-deformed pre-scission shapes of the mother systems, which is supported by the fact that the linear arrangement realizes the lowest Coulomb potential energies of three clusters. We also emphasize, that the Q values for ternary fission are by 25–30 MeV more positive, again due to the formation of magic fragments, than in binary fission. The ternary fission process must be considered to proceed sequentially, with two neck ruptures in a short time sequence characteristic for binary fissions.

6.3 CCT Modes Based on the Deformed Magic Clusters

In the previous sections we have discussed the "Ni"-bump, which is vividly seen in the FFs mass-mass correlation plot without any processing (Fig. 6.4), because it is

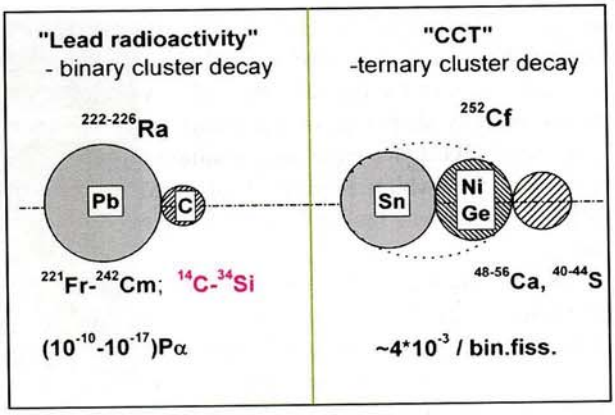

Fig. 6.10 Cluster scheme for the comparison of the lead radioactivity with collinear cluster tri-partition

located below the loci of binary fission. Special analysis of the data from Ex1 let to reveal the bumps based on deformed magic clusters [51, 52]. Two large windows $w1$ and $w2$ were chosen in the mass-mass distribution from Ex1 (Fig. 6.4). The corresponding projections of the distributions onto the coordinate axis in the "clean" arm2 (box $w1$) and those facing to the source backing, arm1 (box $w2$), are compared in Fig. 6.11(a). The spectra were normalized to the same number of counts. The difference spectrum is shown in Fig. 6.11(b). Some statistically significant peaks are seen. The first one from the left is the projection of the "Ni"-bump onto the M_1-axis, this peak was already shown in grater scale in Fig. 6.5. Further structures follow: a wide peak bounded by magic nuclei of ^{82}Ge and ^{94}Kr (deformed), and peaks centering, respectively, at ^{98}Sr and ^{108}Mo isotopes (both to be magic and deformed).

The origin of the peaks becomes clear from following consideration illustrated by Fig. 6.12. Let us focus our attention on the peak in the vicinity of mass 70 amu (Ni) in the difference spectrum (right part of the "Ni"-bump, Fig. 6.11(b)). The fact that the "Ni-bump" is observed only in one of the spectrometer arms facing the source backing, was treated above as being due to a stopping in the entrance mesh of the ionization chamber of the third light fragment directed in the same arm as the Ni cluster. In contrast, the same pair of fragments directed at the "clean" arm2 predominantly (due to a low angular divergence) gives overlapped energy signals in the "stop" detector and time-of-flight signal corresponding to the faster of them. As a result the calculated mass will be incorrect but registered as an "almost normal" binary one within the experimental mass dispersion. Such events from arm2 play a role of "donors" for the bump events in arm1. In other words the events being actually ternary should move from the locus defined as binary in arm2 to the "Ni"-bump in arm1 (illustration in the upper part of Fig. 6.12). As a result the difference spectrum $Y(w2)$–$Y(w1)$ (low part of Fig. 6.12) must have the peak of positive counts and corresponding negative counting tail for the "donors" fragments in the region of binary fission Fig. 6.12. Evidently the yields of the bump and the "tail" must be equal to each other ($S_1 = S_2$).

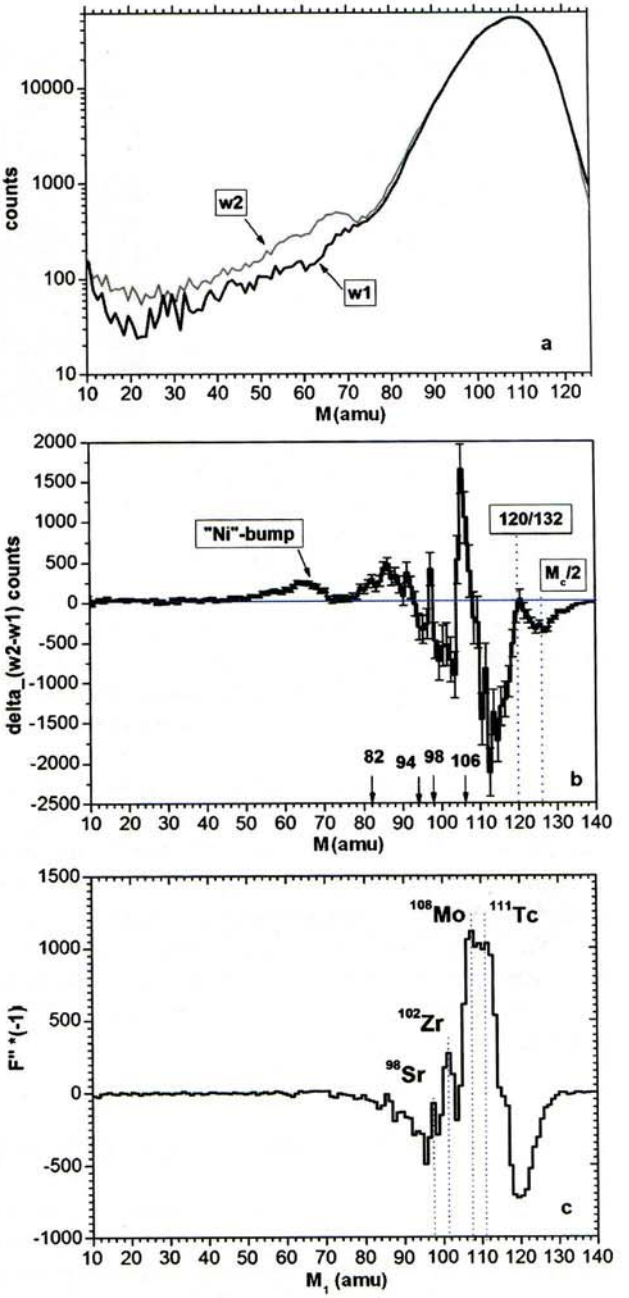

Fig. 6.11 (**a**) Projections of the events from box $w1$ and box $w2$ (Ex1, shown in Fig. 6.1(a)) onto M_2 and M_1 axes, respectively; (**b**) difference between these projections and, (**c**) the second derivative of the spectrum being the projection of the events from box $w2$ onto M_1 axis. See text for details

In the experiment one observes a superposition of partial contributions from different magic clusters. For instance, the gross central peak in Fig. 6.11(b) lies on the negative "background" (tail) provided by all less massive magic clusters.

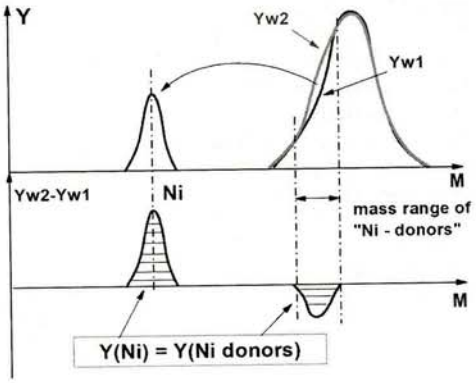

Fig. 6.12 Schematic representation of Fig. 6.8(a) (*upper part* of the figure) for illustrating a reason of forming a negative tail of the "Ni"-bump in the difference spectrum of yields $Y(w2)$–$Y(w1)$ (*lower part*)

The position of the local peaks in Fig. 6.11(b) could depend on a possible shift in the centers of the spectra in Fig. 6.11(a) due to independent mass calibrations in the opposite arms of the spectrometer. We have two independent evidences for the required quality of the calibrations. The maximal mass of the light fragment in the mass-asymmetric fission mode can not exceed 120 amu due to the known extreme stability of the complimentary heavy fragment (double magic ^{132}Sn). This is just the feature observed in Fig. 6.11(b): the negative yield in the difference in the spectrum vanishes for the mass partition 120/132 amu. The negative minimum at $M_c/2$ (Fig. 6.11(b)) where M_c is the mass of the fissioning nucleus of ^{252}Cf, shows, that ternary fragmentation is likely to occur in the region of mass-symmetric fission as well.

Another argument for the quality of the mass calibrations can be inferred from Fig. 6.11(c). The figure shows the second derivative of the mass spectrum linked with the box $w2$ of the data from Ex1, this shows similar peaks as the difference spectrum in Fig. 6.11(b). Thus Fig. 6.11(b) can be treated as a manifestation of a whole sequence of bumps, based on magic spherical and deformed clusters of $^{68-70}$Ni, ^{82}Ge, ^{94}Kr, ^{98}Sr, ^{102}Zr, ^{108}Mo, ^{111}Tc. The yield of the most populated "Mo"-bump ($A = 106$–111) is about 8×10^{-3} per binary fission, i.e. twice as high as the corresponding value for the "Ni"-bump directly seen in the mass correlation plot (Fig. 6.4(a)).

6.4 Ternary Decays with Comparable Masses of the Fragments

When events characterized by approximately equal momenta and velocities were selected in Ex2, the mass-mass distribution of FFs reveals a specific structure in the form of a right angle whose vertex lies on the diagonal of the plot in the vicinity of the points (68, 68) amu (Fig. 6.13(a)). We observed earlier a similar structure (rectangle) in the mass-mass distribution of fragments from the spontaneous fission of the ^{252}Cf nucleus [52].

The assumption that the sides of the right angle in Fig. 6.13(a) are connected with magic Ni isotopes is confirmed by Fig. 6.13(b). It depicts the distribution of FFs with

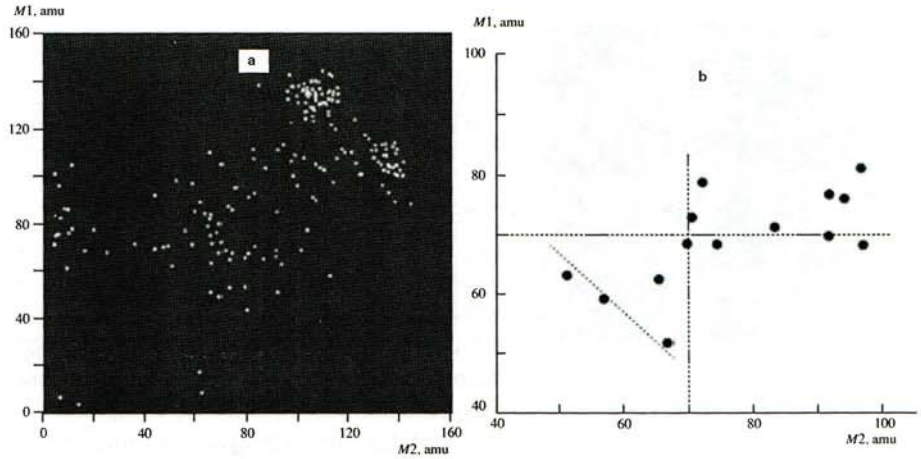

Fig. 6.13 Mass-mass distribution of genetically related FFs with approximately equal momenta and velocities (**b**) the same but also similar nuclear charges are selected. The events at the vertex of the right angle have charges of $Z \sim 28$; the events lying on the slantwise straight line $M_s = \text{const}$ are discussed in the main body of the text

approximately equal momenta, velocities, and nuclear charges. With allowance for a small shift toward larger values in the charge calibration in arm 1 [53], a charge of about 28 does indeed correspond to the points at the vertex of the angle. Of interest in this figure are also points that lie on the slantwise straight line $M_s = \text{const}$, and the "lost" mass corresponds here to the deformed magic nucleus ^{118}Pd. The middle of the points corresponds in mass and charge to a symmetric pre-scission configuration of three magic clusters: ^{59}V–^{118}Pd–^{59}V.

Note that, although the distribution in Fig. 6.13(b) includes just a few events, the reliability of their analysis is quite high. Indeed, there are no other points in the vicinity of the concentration of points under consideration. Each point results from the measurement of six independent experimental parameters (time-of-flight, energy, and drift time at each arm). Finally, the points are grouped along three specific directions: M_1, $M_2 = \text{const}$, and $M_s = \text{const}$.

A less stringent selection permitted revealing a whole family of events similar to the three-cluster configuration discussed above. Figure 6.14(a) shows the distribution of FFs upon momentum and drift time selections. The momentum selection was applied to events in the rectangular window shown in Fig. 6.14(b). It includes events beyond the tails resulting from scattering of FFs by the supporting grid of the BIC entrance window. The second window includes events characterized by an increased value of the parameter D on the V-D matrix. The most intense concentrations of points in Fig. 6.14(a) remained from the loci of ordinary binary fission. The points indicated by the arrow and situated on the straight line $M_a = M_b$ stand out among others. They are separately shown in Fig. 6.14(c). The mass distribution of detected fragments in Fig. 6.14(c) gives sufficient grounds to assume that the corresponding pre-scission configurations are three-body chains comprising two or

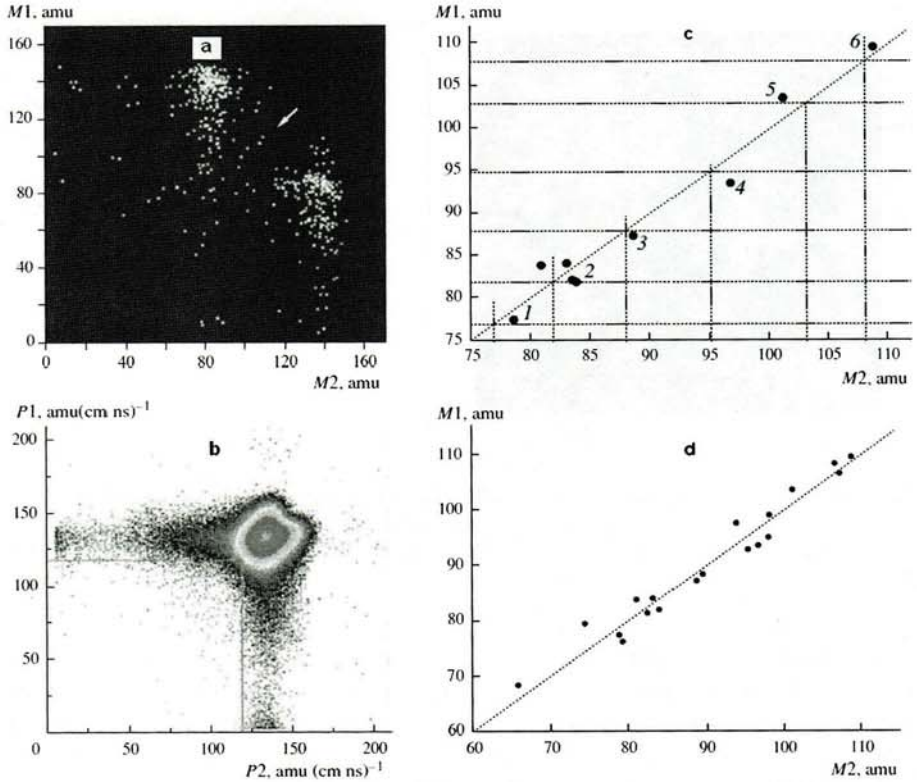

Fig. 6.14 (**a**) Mass-mass distribution of FFs selected by the momentum and the parameter D_{exp}. The arrow points to the group of events with approximately equal masses. (**b**) Window (rectangle) for selection in the momentum wP in the momentum-momentum distribution of FFs. (**c**) Events of collinear cluster tripartition with equal masses of detected decay products. The *numbers* label the following cluster configurations: (1) $^{78}Zn_{30}$–$^{80}Ge_{50}$–^{77}Zn, (2) $^{82}Ge_{50}$–$^{72}Ni_{28}$–^{82}Ge, (3) $^{88}Se_{54}$–$^{60(2)}Cr_{24}$–^{88}Se, (4) $^{95}Rb_{58}$–$^{46}Ar_{28}$–^{95}Rb, (5) $^{103}Zr_{40}$–$^{30(2)}Mg$–^{103}Zr, and (6) $^{108}Mo_{66}$–^{20}O–^{108}Mo. (**d**) As in Fig. 6.14(c), but for total statistics

three magic clusters. As statistics increase, the population of the region along the straight line $M_a = M_b$ also increases (Fig. 6.14(d)), and the yield of these events was 8×10^{-6} (binary fission)$^{-1}$.

6.5 CCT with Light Ion Emission

It is known that the drift time of the track formed by the fragment in the chamber gas to the Frisch grid is associated with the nuclear charge of the fragment [37, 54]. The corresponding parameter D_{exp} was measured as the difference between the time signal from the position sensitive avalanche counter and the time reference for the pulse front from the Frisch grid of the Bragg ionization chamber. The mass,

energy, and track drift time measured for each fragment were used to find the nuclear charge of the fragment Z with the help of a specially developed procedure [38]. Note that for the investigation of multi-body (not binary) decays, only the mass of the fission fragment calculated via its velocity V (time-of-flight T) and energy (E) can be used. The determined mass is thus denoted below as M_{TE}, unlike the mass M_{TT} calculated via fission fragment velocities.

The main background for the investigated effect is given by fragments scattered on the input grid of the Bragg ionization chamber. These are characterized by lower M_{TE} values but correctly measured velocities and correspondingly, M_{TT} masses. The track drift time in the Bragg ionization chamber, D_{exp}, is also measured correctly. Due to the above, it is entirely possible to distinguish between the investigated effect and the scattered events of binary fission. To accomplish this, a formula associating the drift time, mass, and charge of the ion from [38] is used to introduce the additional variable of calculated drift time:

$$D_{calc} = \alpha - \beta\sqrt{E_{BIC} M^*_{TT} Z^{-2/3}} + \gamma M^*_{TT} Z^{-2/3} \tag{6.1}$$

where M^*_{TT} is the mass corrected to the number of emitted neutrons, i.e., the "post-neutron" (M) mass; Z is the fragment charge corresponding to the hypothesis of constant charge density (Z_{UCD}); E_{BIC} is the fragment energy in the Bragg ionization chamber; and α, β, γ are the parameterization coefficients found a priori using charge calibration.

It follows from definition of D_{calc} (6.1) that for scattered events $D_{calc} = D_{exp}$ within resolution, and for events of collinear cluster tri-partition $D_{calc} > D_{exp}$. This can be proved by comparing D_{calc} for a typical light fragment registered correctly and after scattering, respectively. The distribution of D_{calc}–D_{exp} for one spectrometer arm obtained in Ex2 is shown in Fig. 6.15(a). The nuclear charge distribution of fission fragments for events beyond the triangular window in Fig. 6.15(a) (i.e., increased values of D_{calc}) is shown in Fig. 6.15(b). Arrows mark groups of events with small charges to be further analyzed.

The spectra of masses, charges, velocities, and energies for these ions are shown in Fig. 6.16.

Note first of all that the discussed data are related to almost collinear tri-partition of $^{236}U^*$ nucleus due to the limited spectrometer aperture, thus the maximum deviation of the lightest fragment from the fission axis cannot exceed 14°. It follows from Fig. 6.15(b) that almost in all analyzed events the light ion (light charged particle) is registered in coincidence with a fragment from the light group of mass distribution of fission fragments observed in conventional binary fission. In this case, the heavy fragment flying in the same direction as the light charged particle either goes beyond the spectrometer aperture (case a) or is lost at the input grid of the Bragg ionization chamber (case b). This follows, e.g., from Fig. 6.17(a) for events marked in Fig. 6.15(b) by vertical arrow. In case *a*, the heavy fragment has not hit the position sensitive avalanche counter and the signal dE is given by the light charged particle only (the lower group of points). If both the light charged particle and the heavy fragment pass through the counter the signal dE is considerably larger (the

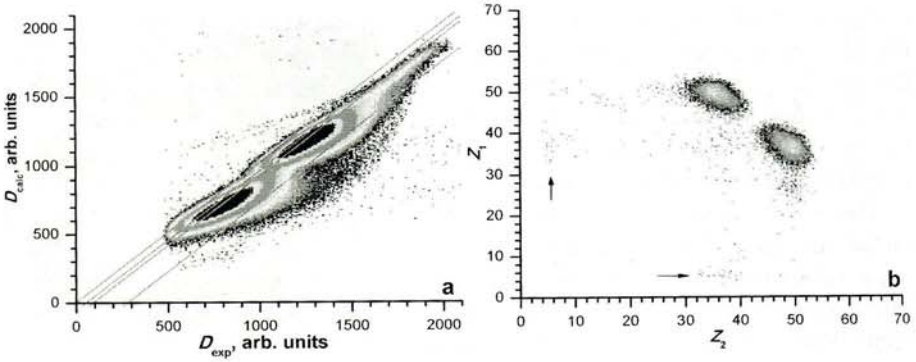

Fig. 6.15 (**a**) Distribution $D_{calc}-D_{exp}$ in one of the spectrometer arms; (**b**) nuclear charge distribution of fission fragments for events beyond the triangular window in (**a**). See the text for detailed description

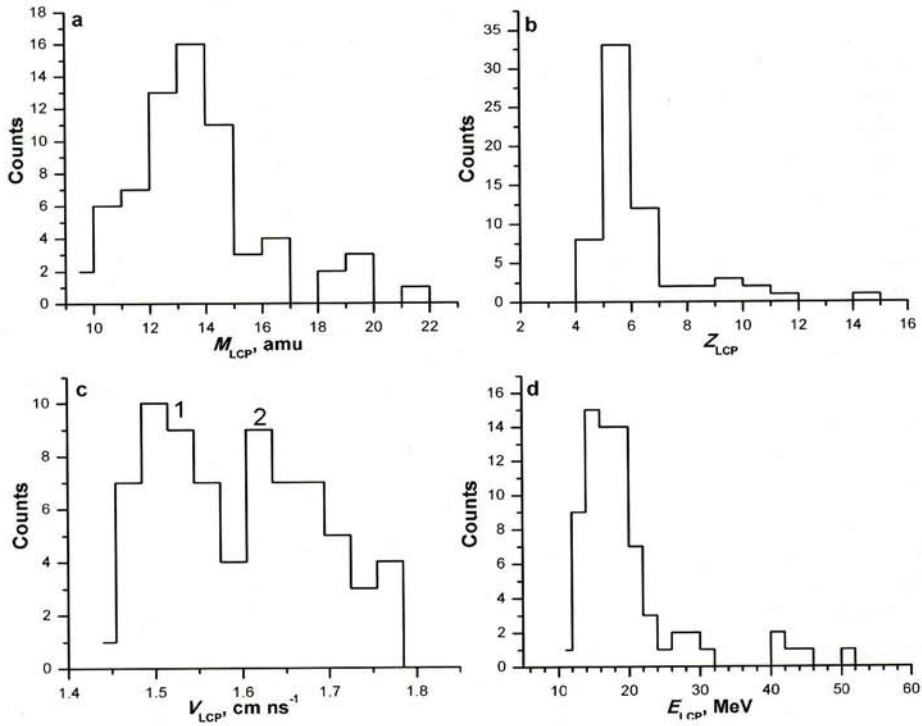

Fig. 6.16 Spectra of (**a**) masses, (**b**) charges, (**c**) velocities, and (**d**) energies of light ions marked by *arrows* in Fig. 6.15(b)

upper group of points), however, then the heavy fragment is lost at the input grid of the Bragg ionization chamber and only the light charged particle is registered.

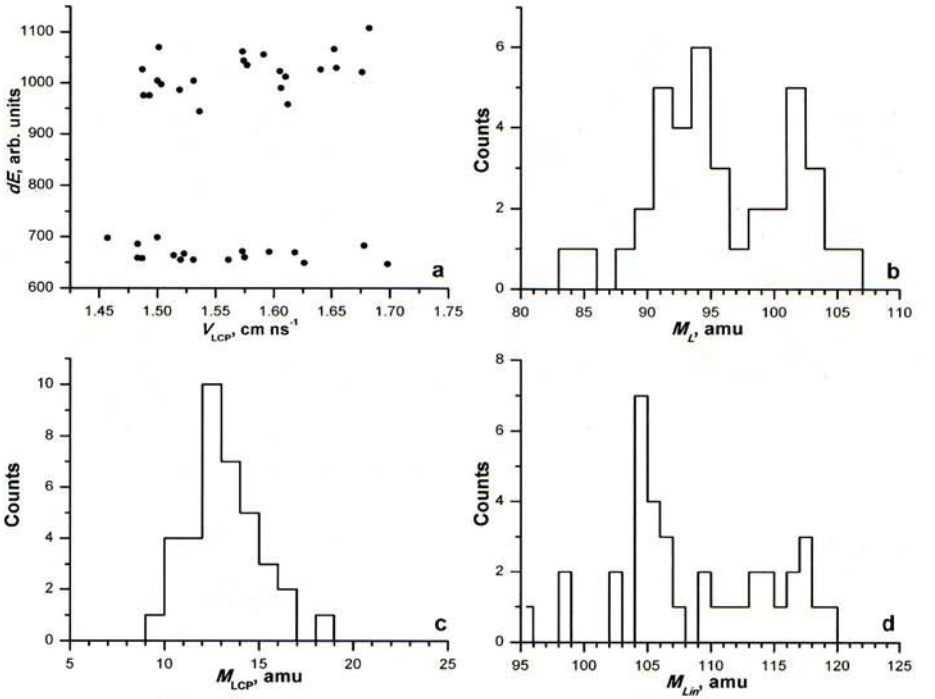

Fig. 6.17 (**a**) Distribution velocity-energy loss in the position sensitive avalanche counter for fragments in the first spectrometer arm; (**b**) mass spectrum of light fragment registered in coincidence with light charged particle with the velocity $V_{LCP} < 1.6$ cm ns^{-1} (peak 1 in Fig. 6.16(c)); (**c**) mass spectrum of such light charged particles; (**d**) mass spectrum of light fragments before light charged particle partition

Two groups of ions can be seen in the velocity spectrum of light charged particles (peaks 1 and 2 in Fig. 6.16(c)). The spectrum of masses (M_L) of light fragments measured in coincidence with these light charged particles from the first peak ($V_{LCP} < 1.6$ cm ns^{-1}) is shown in Fig. 6.17(b). It consists of two peaks associated with magic nuclei ^{94}Kr and ^{103}Zr (shell minimum "B" of the map of shell corrections from Ref. [45] and shell minimum for $Z = 40$ from Ref. [55], respectively). The mass spectrum of light fragments (M_{Lin}) before the partition of the light charged particle is of interest. To obtain this spectrum, the masses were summed event-wise, $M_{Lin} = M_L + M_{LCP}$. The mass spectrum of the light fragment prior to light charged particle partitioning is shown in Fig. 6.17(d). The central mass peak corresponds to the magic isotopes ^{105}Zr–^{106}Nb (shell minimum "C" from Ref. [45]).

The total spectrum of primary masses of light fragment M_{Lin} is shown in Fig. 6.18 (on the left of the central separating line corresponding to $M_c/2$, where M_c is the mass of the compound nucleus). Along with the peak in a mass region of ~106 amu, the second peak is observed for 111–113 amu; this peak is associated with the deformed magic nuclei ^{111}Tc and ^{113}Ru (shell "C" [45] and its experimental manifestation discussed in Ref. [56]). The mass of the lost heavy frag-

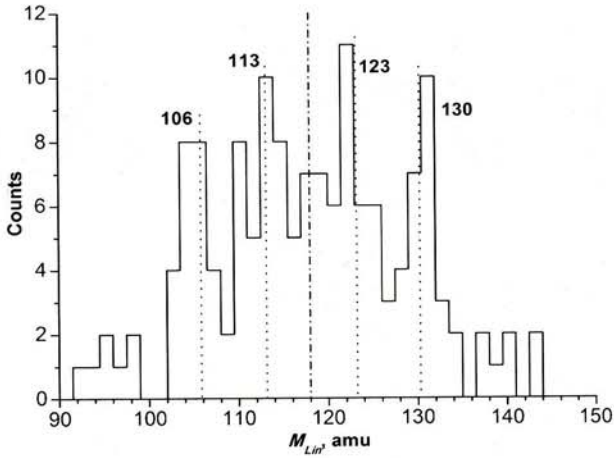

Fig. 6.18 Masses of fragments at the binary stage of fission; the *dashed-and-dotted line* corresponds to one half the mass of the compound nucleus

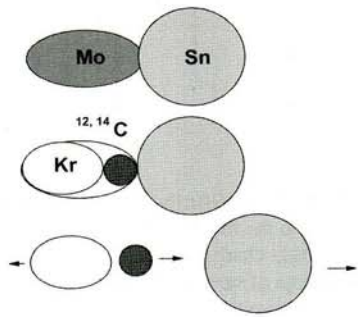

Fig. 6.19 Illustration of the scenario of collinear cluster tripartition

ment can be reconstructed, $M_H = (236 - M_{Lin})$ amu. The peaks in the spectrum of heavy fragments (Fig. 6.18) correspond to magic ^{123}Cd (shell "K" [45]) and ^{128,132}Sn.

The obtained experimental information can be generalized in the context of the following scenario of the two stage decay of ^{236}U*. Being sufficiently elongated, the system clusterizes, forming the di-nuclear system (Fig. 6.19) consisting of two magic clusters. Upon further elongation, the deformed light magic cluster (Mo) clusterizes into light charged particle (carbon nucleus) and the magic remainder (Kr).

The process of collinear cluster tri-partition according to a similar scenario in ^{236}U* may take place both in valleys of mass-asymmetric and mass-symmetric forms [57]. To the best of our knowledge, the described effect was not observed earlier in works on the polar emission of light charged particles, this is probably associated with the excessive thicknesses of the *dE* detectors used to identify the charge of light charged particles.

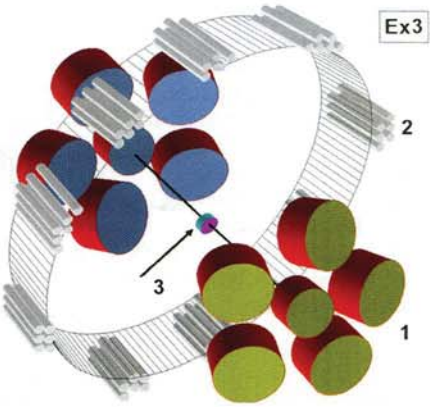

Fig. 6.20 Layout of the experiment (Ex3) for the neutron coincidences with the modified spectrometer based on FOBOS detector modules (*1*), the "neutron belt" consisting of 140 ^{3}He-filled neutron counters (*2*), and the "start" avalanche counter with the Cf source inside (*3*)

6.6 Additional Information from the Neutron Gated Data

6.6.1 Experiment Ex3

Results of two different experiments (Ex3 and Ex4) for the study of fission of ^{252}Cf (sf) events in coincidence with neutrons are reported in this section [58]. The experiment (Ex3) has been carried out with the modified FOBOS spectrometer also at the FLNR of the JINR. The layout of the experimental set-up is shown in Fig. 6.20. Due to the low yield of the process under study, a compound configuration containing five big and one small standard FOBOS modules in each arm was used. The distance to the source is again 50 cm. Such a scheme of the double-armed TOF-*E* spectrometer allows the measurement of energies and velocity vectors of the coincident fragments and covers ~16 % of the hemisphere in each arm. In order to provide "start" signals for all of the modules only wide-aperture start detectors capable to span a cone of ~100° at the vertex could be used. Another point to be taken into account when choosing appropriate start detectors, arises from the expected decay kinematics (Fig. 6.1, insert b). Among two fragments flying in the same direction only the faster one will be assigned a correct TOF, if the start detector is located at some distance from the decay source. Both problems are solved in the specially designed very compact three-electrode start avalanche counter, in which the central electrode (cathode) is combined with the ^{252}Cf fission source (330 fissions/s, and a Al_2O_3 backing of 50 μg/cm^2 thickness).

From the results of our previous experiments we can assume, that there are several CCT modes [33] with the middle fragment of the three-body pre-scission chain with very low velocity after scission. The neutrons emitted from the moving binary fission fragments are focused predominantly [59] along the fission axis. In order to exploit this directivity for revealing the CCT events, the "neutron belt" was assembled in a plane perpendicular to the symmetry axis of the spectrometer, which serves as the mean fission axis at the same time (Fig. 6.20) [60]. The centre of the belt coincides with the location of the fission source. The neutron detector consists of 140 separate hexagonal modules each comprising ^{3}He-filled proportional

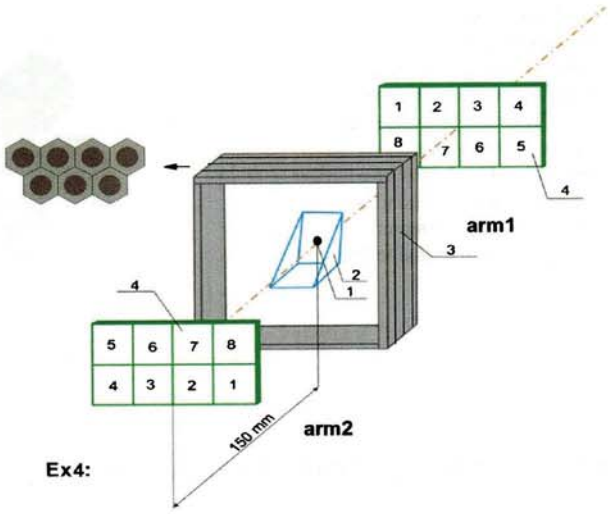

Fig. 6.21 Scheme of the COMETA set-up of Ex4, which consists of two mosaics of eight PIN-diodes each (*4*), the MCP based start detector (*2*) with the ^{252}Cf source inside (*1*), and the "neutron belt" (*3*) consisting of 28 ^{3}He-filled neutron counters in a moderator. The cross section of the belt is marked by the *arrow*

counter, a moderator, a high-voltage input and a preamplifier. The counters operate under a gas pressure of 7 bar, being 50 cm in length and 3.2 cm in diameter. The moderator is made of polyethylene. The neutron counters cover altogether ~29 % of the complete solid angle of 4π. The "neutron belt" consists of two layers of neutron registration modules. At the testing stage we have found that more than 90 % of the neutrons were detected in the two first layers of the counters. For this reason the third layer was omitted in the final version of the set-up.

The registration efficiency for neutrons does not exceed 4 % for those emitted in normal binary fission and it is 12 % for neutrons emitted isotropically. The electronics of the "neutron belt" is operated in slave mode being triggered by the fission event selector. All in all more than 2×10^6 fission events in coincidence with neutrons were detected.

6.6.2 *Experiment Ex4*

The experiment Ex4 has been performed as the two previous ones at the FLNR of the JINR using the COMETA set-up (Fig. 6.21). It is the double arm TOF-E spectrometer which includes the micro-channel plate (MCP) based "start" detector with the ^{252}Cf source inside, similar to that used in Ex2. Two mosaics of eight PIN diodes each served as the stop detectors and the "neutron belt" comprising 28 ^{3}He-filled neutron counters are used. Each PIN diode (2×2 cm of surface area) provides both energy and timing signals. The actual active area of the PIN diodes is a little bit smaller due to the multi-aperture diaphragm, non-transparent for the FFs, covering the mosaic as a whole. The diaphragm provides ~3 mm demarcation strips between neighbouring diodes. Thus the angle between the fragments L_1 and L_2 (see Fig. 6.1(b)) must be more then 1° in order them to be detected in neighbouring

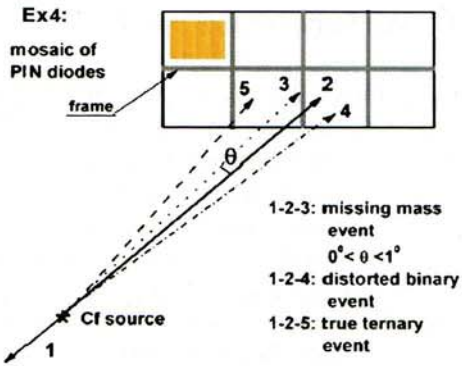

Fig. 6.22 Geometry in Ex4 with the PIN diodes. Hitting the mosaic by a fork of fragments can give rise to three different types of events. Blocking can occur if the opening angle of the fork lies in the range $0° < \theta < 1°$ (missing mass event marked as 1–2–3). Both fragments of the fork can hit the same PIN diode (event 1–2–4). If $\theta > 1°$ the fragments forming the fork can be detected in two different PIN diodes (true ternary event 1–2–5)

diodes. In this way the structure provides a dead-zone, where one of the fragments can get lost (similar to Ex1, Fig. 6.1(b)). Each flight path is 15 cm.

The use of the Si-semiconductor detectors in TOF-E spectrometry of heavy ions (or FFs) is known to have delicate methodological problems due to the "amplitude (pulse-height) defect" [61] and "plasma delay" [62] effects in the E and TOF channels, respectively. The first effect involves a nonlinearity in the dependence of the deposited energy on the electrical charge measured, while the latter distorts the TOF used in the calculation of the heavy ion masses. We have worked out an original approach for accounting of the amplitude defect and the correct reconstruction of the FF mass in TOF-E measurements [63]. Unfortunately, it is valid only for the case when dispersion of the plasma delay time can be ignored due to a long flight path used. This is not the case here.

To overcome the problem we have used a simplified approach as follows. Two coefficients of the linear time calibration are calculated using the velocity spectrum of the known FFs from the literature. The energy calibration dependence is presented as a parabolic curve passing via three points, namely, through the known centres of the energy peaks for the light and heavy fragments, and the energy of the alpha-particles of the natural radioactivity of ^{252}Cf nucleus. Such approach gives quite satisfactory results for the reconstruction of the FF masses, at least, in the vicinity of the loci of binary FFs, as shown below.

The neutron belt is located in the plane perpendicular to the symmetry axis of the set-up. According to modelling and previous experiments, the detection efficiency is estimated to be ~5 % and ~12 % for the neutrons emitted in binary fission and from an isotropic source, respectively [64]. The total statistics of binary fission events collected for Ex4 in coincidence with neutrons is about 4×10^6.

6.6.3 *Efficiency for the Registration of CCT Events*

The registration of the CCT events is based on the double arm time of flight and energy (TOF-E) measurements and the particular geometrical blocking effect, already introduced in Refs. [33, 51] which are shown in Fig. 6.1. In this section we give a discussion of the geometrical differences of the three experiments. These are partially contained in the description of each experiment. We summarise that the missing mass approach is linked both to the blocking of parts of the solid angle of the E-detectors and the dispersive effect of the backing of the source. For the two collinear (relative angle 180°) fragments, which come from the first neck rupture, as in binary fission, one is reaching the energy detectors undisturbed ($A1$). For the second neck rupture of the other fragment ($A23$), again two fragments ($A2$ and $A3$) are produced collinearly, however, these are dispersed in the backing of the source and in other media (start detectors), into a fork with a certain opening angle. In Ex1 and Ex2 the support grid of the gas-ionisation chambers act as blocking medium over the whole area of the solid angle of the ionisation chambers. In Ex3 these are the narrow regions around the frames defining the solid angle of the E-detectors (PIN diodes), see Fig. 6.22. A fork of two fragments, hitting the mosaic detectors can give rise to three different types of events.

- Blocking can occur if the opening angle of the fork lies in the range $0° < \theta < 1°$ (missing mass event marked as 1–2–3 in Fig. 6.22). As a consequence only an area along the border lines of the PIN diodes is available to register CCT events with a missing mass. The opening angle of the fork θ is expected to be around 1° [54]. In the actual geometry of Ex4 approximately 60 % of the whole area of each PIN is active for the registration of one of the fragments in the fork in such scenario.
- Both fragments of the fork can hit the same PIN diode (event 1–2–4 in Fig. 6.22). In this case the masses of the fragments are not correctly determined. An interesting manifestation of such events will be discussed below in Sect. 6.6.7.
- If $\theta > 1°$ the fragments forming the fork can be detected in two different pin-diodes (true ternary event 1–2–5 in Fig. 6.22).

In order to define the differences in the structures of the M_1–M_2-plots, we can use an expression which defines the experimentally observed yield Y_{exp_CCT} of a distinct CCT mode. It can be estimated as follows:

$$Y_{exp\_CCT} \sim Y_{phys} \times P_{miss}. \tag{6.2}$$

Here Y_{phys} is the relative (per binary fission) physical yield of the corresponding collinear ternary decay mode, P_{miss} is the probability that one of the CCT partners will be lost while two others are detected, defining the missing mass approach.

Further for neutrons in coincidence (in Ex3 and Ex4), P_n defines the probability to register n neutrons in coincidence with the FFs from the CCT decay. For this case Eq. (6.2) must be amended as follows:

$$Y^n_{exp\_CCT} \sim Y_{phys} \times P_{miss} \times P_n. \tag{6.3}$$

For Ex1 the opening angle of the fork must be larger than 0.15° in order that one of the fragments gets blocked. For Ex3 this angle is very similar. The blocking structure in these experiments is homogenously distributed over the whole solid angle. For Ex4 this condition is quite different, the blocking medium is determined mainly by the spaces between the adjacent PIN diodes, which is given by the frames. The efficiency to register a blocking event is a factor 3 smaller.

6.6.4 Inclusive Data for the Experiments Ex1, 3, 4

The analysis is based on the presentation and discussion of two-dimensional diagrams of the registered masses (M_1 and M_2), in which the sum M_s of the two masses can be discussed. The events with total masses $M_s = M_1 + M_2$ will appear as diagonal lines in the mass correlation plot. Projections onto an axis showing either M_1 or M_2, are also used. Rectangular-like structures bounded by the magic nuclei will be shown as well. These are well seen for higher neutron multiplicities in the neutron gated data (Sect. 6.6.5).

6.6.4.1 Experiment Ex1

We repeat shortly the results reported in Sect. 6.2. The most pronounced manifestation of the CCT as a missing mass event is a bump (Fig. 6.4) in the two dimensional mass-mass correlation plot. In this distribution of the fission fragment masses, the bump occurs only in one of the spectrometer arms with dispersive media (M_1), whereas it is absent in the analogues variable for the second arm (M_2). The bump is marked by the arrow in Fig. 6.4. We see two great peaks due to binary fission, the pronounced vertical and horizontal intensities are due to binary fission fragments scattered on the entrance support grid for the windows of the gas detectors (see Fig. 6.1). Actually this background becomes negligible in Ex4.

6.6.4.2 Experiment Ex3

The inclusive results as obtained in the experiment Ex3 (Fig. 6.20) (with lower statistics) confirm the results of Ex1. New aspects are obtained by gating the FF mass-mass distributions by the number of neutrons detected in coincidence (Sect. 6.6.7), see also Ref. [65].

At first we will compare the results of Ex3 without neutron gating, with those obtained in Ex1. The FF mass correlation plot, similar to that obtained in Ex1 (Fig. 6.4 is shown in Fig. 6.23(a). Projections of this distribution both on the M_1 axis and on the M_s directions are presented in Fig. 6.23(b), and 6.23(c), respectively. They are compared with the analogous spectra from the experiments Ex1, including the result (Ex2) from the $^{235}U(n_{th}, f)$ reaction [49].

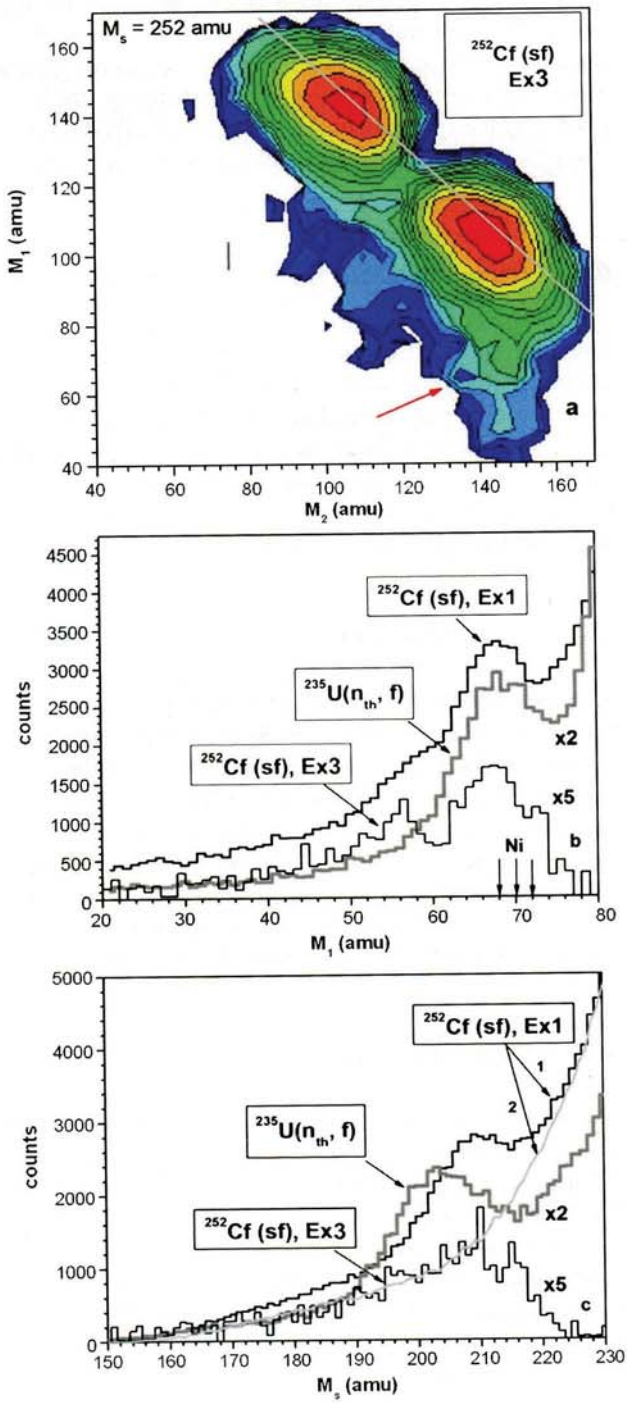

Fig. 6.23 (**a**) Contour map of the mass-mass distribution (logarithmic scale, with lines approximately a step factor of 1.5) from a coincidence in the two opposite arms of Ex3. The bump in the spectrometer arm (arm1) facing the backing of the Cf source is marked by the *arrow*. (**b**) Projections onto the M_1 axis for comparison with the experiment Ex1, and with the Ex2 results of the $^{235}U(n_{th}, f)$ reaction [49]. Positions of the magic isotopes of Ni are marked by the *arrows* (see text of Sect. 6.6.4.3 for details). (**c**) Projections onto the direction $M_s = M_2 + M_1$. The result for Ex1 is presented by two curves marked by the *arrows 1* and *2* (*dotted*) for the arm1 and arm2, respectively. For Ex3 the yield of arm2 is subtracted

The bump in the projected FF mass correlation data in Fig. 6.23(b) is located around magic isotopes of Ni, these are the isotopes of ^{68}Ni, ^{70}Ni and ^{72}Ni having the magic number of protons $Z = 28$. The first one can be called a "one and a half" magic nucleus due to the neutron sub-shell $N = 40$ [46, 66], while the last one has nucleon composition corresponding to the unchanged charge density hypotheses (Z_{UCD} hypotheses) [67–69]. The middle isotope of ^{70}Ni showing enhanced yield in far asymmetric fission [46] is likely a compromised version in between two already considered nuclei. This bump will be called below as the "Ni"-bump. The bump marked by the arrow in Fig. 6.23(a) looks less pronounced as compared to that obtained in Ex1 (Fig. 6.4). This can be partially explained by a worse mass resolution due to a larger total thickness of the foils along the flight pass (see Sect. 6.6.6 for details). Projections for Ex3 are shown in the "difference" version, i.e. as a difference of the tail regions in arm1 and in arm2, respectively. The second peak at lower masses in Ex3 looks more pronounced, it corresponds to the complicated two-dimensional structure centered at $M_1 \sim 56$ amu in Fig. 6.27. Overall a good agreement is observed in the position of the peaks in Fig. 6.23(b), and 6.23(c) for all three experiments. The shift of the peak for the ^{235}U(n_{th}, f) reaction in Fig. 6.23(c) has already been discussed in Ref. [54].

6.6.4.3 Experiment Ex4

This methodically quite different experiment confirms our previous observations concerning the structures in the missing mass distributions. In this case there is no tail due to scattering from material in front of the E-detectors. Figure 6.24(a) shows the region of the mass distribution for the FFs from ^{252}Cf (sf) around the "Ni"-bump ($M_1 = 68$–80 amu, $M_2 = 128$–150 amu). The structures are seen in the spectrometer arm facing the source backing only. No additional selection of the fission events has been applied in this case, the experiment has no background. A rectangular-like structure below the locus of binary fission is bounded by magic nuclei (their masses are marked by the numbered arrows), namely, ^{128}Sn (1), ^{68}Ni (2), ^{72}Ni (3). In Fig. 6.24(b) we show the projection of the linear structure seen at the masses 68 and 72 amu. Peaks seen in Fig. 6.24(b) allow to estimate a mass resolution of the COMETA set-up to be < 2.0 amu (FWHM).

Two tilted diagonal lines with $M_s = 196$ amu and $M_s = 202$ amu (marked by number 4) start from the partitions 68/128 and 68/134, respectively. In experiment Ex1 [51], Fig. 6.6, similar sub-structures have been seen for masses $M_s = 204$, 208, 212, 214 amu, where they were revealed indirectly—by applying a method of the second derivative filter to the absolutely statistically reliable distribution. We emphasize the difference in the geometry of the blocking mediums in Ex1 and Ex4, which are decisive for the relative experimental yields of the CCT modes with different angular distributions between the fragments forming the fork (see Sect. 6.6.3). We

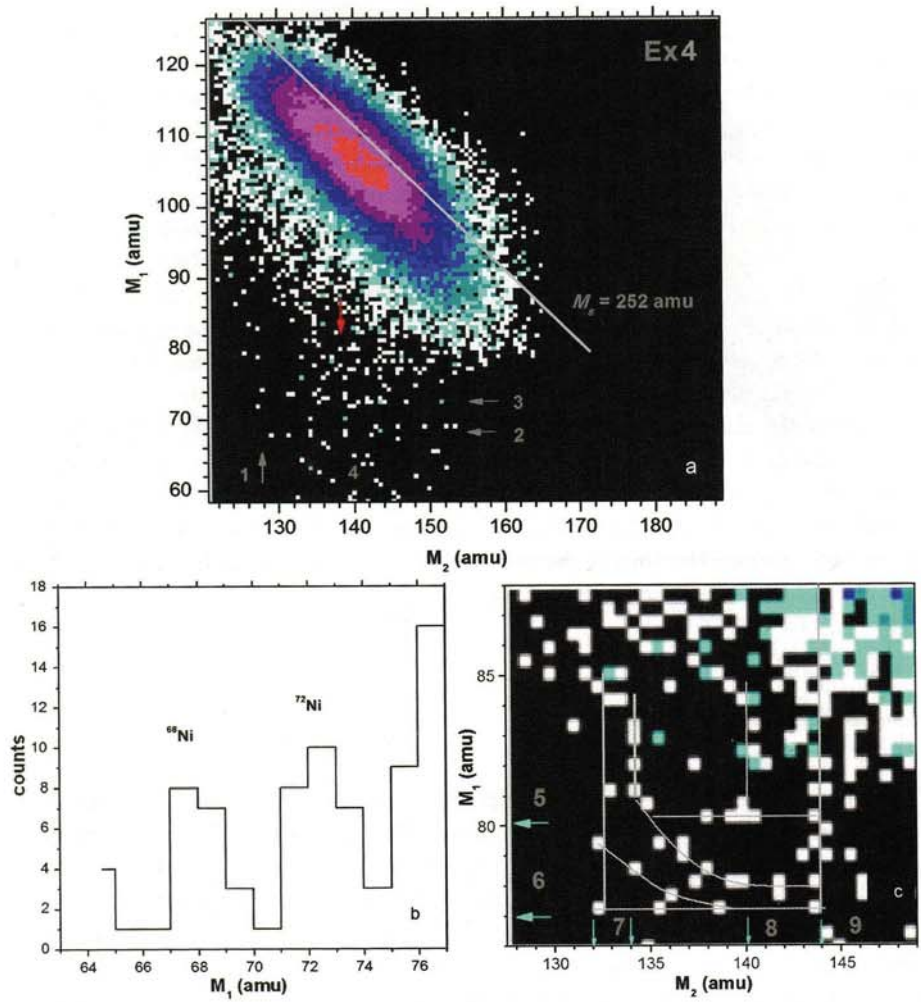

Fig. 6.24 Results of Ex4: The region of the mass-mass distribution for the FFs from ^{252}Cf (sf) around the CCT-bump (Figs. 6.4 and 6.23(a)). No additional gates were applied since there is no background of scattered fragments due to the use of PIN-diodes. An internal structure of the "bump" seen as the *horizontal lines* marked by the *arrows 2* and *3* is shown in Fig. 6.24(b) as a projection. A part of the plot just below the locus of binary FFs yielding the rectangular structure marked by the *red arrow* in part (**a**), already seen before, is shown in a larger scale in (**c**). The *lines* are drawn to guide the eye

observe the preference of lighter mass partitions which produces the tilted ridges in Ex4. The positions of the points in the lower part of Fig. 6.24(a) confirm the possible existence of the ridges revealed in Ex1, with the following magic partitions assigned to the starting point of the ridges: 70/134 ($M_s = 204$ amu), 68/140 ($M_s = 208$ amu), 68/144 ($M_s = 212$ amu), 70/144 ($M_s = 214$ amu).

Thus, the comparison of Ex1 and Ex4, which are very different both by the structure of the detectors and the mass calculation procedures used, as well as the statistics collected, still gives a strong confirmation of the existence of tilted ridges $M_S = \text{const}$ linked with magic partitions. As can be inferred from Fig. 6.24(a), the yield of the FFs with the mass 128 amu, which is extremely low in conventional binary fission, is clearly seen. The scattered binary fragments can not give rise to this structure. A part of the plot just below the locus of the binary FFs for a little bit lower statistics is shown in a larger scale in Fig. 6.24(c). The structure is bounded by the magic nuclei of ^{80}Ge, ^{77}Zn, ^{132}Sn, ^{144}Ba (their masses are marked by the arrows 5, 6, 7, 8, respectively). According to the shell correction map from [55] the nucleon composition of the ^{77}Zn isotope corresponds to a deformed shell for both neutrons and protons. The stabilizing effect for mass numbers around $A = 76$ in conventional ternary fission is reported in Ref. [70]. The structures observed in Fig. 6.24 agree in most aspects with the rectangular structures seen in the neutron gated data of Ex3.

These observations point to the fact that the CCT decay occurs in a large variety of modes (mass combinations), which could not be distinguished in Ex1 without additional gating due to the large background from scattered FFs.

Likely due to the difference in the parameters of the blocking mediums, the experimental yield of the "Ni"-bump in Ex4 does not exceed 10^{-3} per binary fission, i.e. it is much less then in Ex1 and Ex3. At the same time with the absence of scattered FFs in Ex4, we were able to observe the internal structure without any additional cleaning of the FF mass distribution.

6.6.5 *Results of Neutron Gated Data for the Experiments Ex3 and Ex4*

The spectrum of the measured neutron multiplicities is presented in Fig. 6.25. For comparison, a similar spectrum, but measured in a 4π geometry and calculated for an efficiency of 100 % with corrections from Ref. [65], is shown in the insert (a) of this figure. Actually the experimental neutron-multiplicity spectrum in our experiments is formed as a superposition of several components. Each partial neutron multiplicity (panel a) is transformed according to the binomial law and contributes to the experimental neutron-multiplicity spectrum. During the time gate opened by a fission event for reading the neutron counters, those neutrons from previous fission events as well as neutrons from the background of the experimental hall can give additional contributions to the number of neutrons detected. These two sources have been calculated in the frame of the model of the neutron registration channel [60] and they are shown in Fig. 6.25 (the curves marked as "pile-up" and "background"). The model with the parameters known both from the experiment [71] and from the simulations using the MCNP code [72] reproduces the experimental data very well.

It should be stressed that experimental neutron multiplicities in our work are used for gating of the coincident fission fragments only. Reconstruction of the absolute neutron yields, similar to those shown in the insert of Fig. 6.26 is quite a different task beyond the scope of this work.

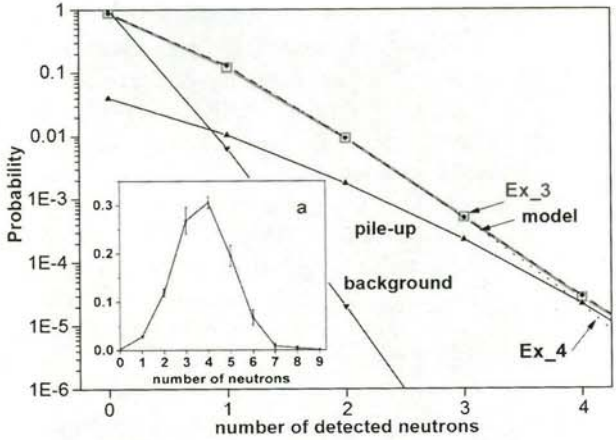

Fig. 6.25 Neutron multiplicities measured in Ex3 (*gray rectangles*) and Ex4 (*dotted line*) in coincidence with fission fragments. The error bars do not exceed the dimension of the symbol. Calculated multiplicities for Ex3 are shown by a *dashed line* (marked as "*model*"). Contributions of the background and pile-up events in Ex3 are marked as "*background*" and "*pile-up*", respectively. *Panel-insert* (**a**) depicts the spectrum of neutron multiplicities for ^{252}Cf (sf) from Ref. [65] measured in 4π geometry and recalculated to a registration efficiency of 100 %

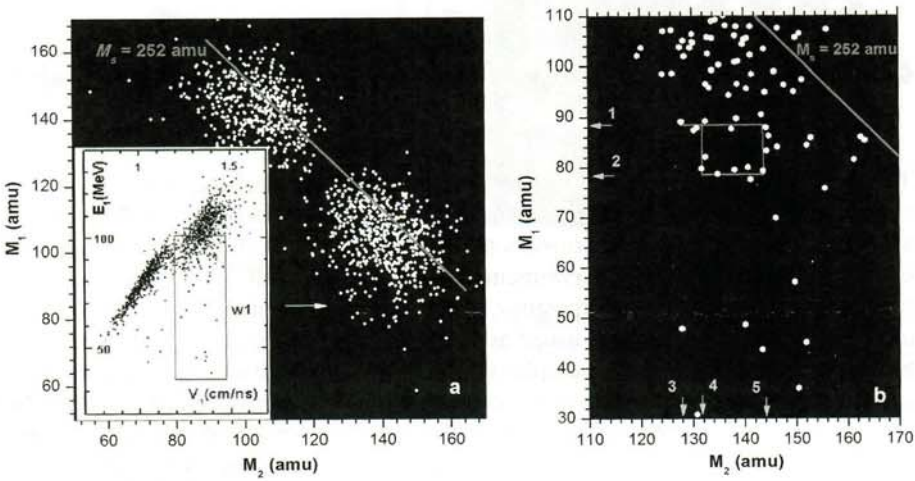

Fig. 6.26 Results of Ex3 ($n = 3$): (**a**) Mass-mass distribution of the FFs for the multiplicity $n = 3$. The rectangular structure is marked by the *arrow*. (**b**) Mass-mass plot for the events in Ex3 with $n = 3$ and the gate $w1$ in the V_1–E_1 plot shown in the insert. The rectangular structure in the plot is bounded by the magic numbers in nuclei with the masses M_2: 132–144 amu and M_1: 78–88 amu, these are marked by the *arrows*. The *lines* are drawn to guide the eye. See text for additional details

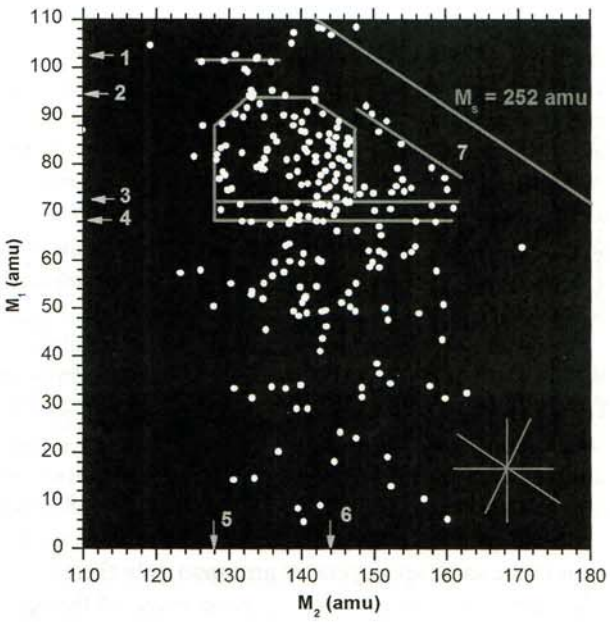

Fig. 6.27 Ex3: results for neutron multiplicity $n = 2$. The mass-mass distribution of the FFs is accumulated with the additional gate $w1$ as in Fig. 6.26(a) in the V_1–E_1 plot. This diagram contains no background from scattered particles. *Arrows with the numbers 1–6* mark the positions of masses of magic nuclei, the *line numbered 7* points to events with the loss of a ^{14}C nucleus, as discussed below. The main intensity corresponds to the masses for the third fragments from 36 down to 20. The *lines* are drawn to guide the eye. See text for more details

6.6.5.1 Experiment Ex3

As mentioned before in Sect. 6.6.1, the experiment under discussion with coincident neutrons was motivated by the expectation that the central fragment is connected to an isotropic neutron source of increased (as compared to binary fission) multiplicity linked with the CCT. For this reason a selection of the fission events with an increased number of detected neutrons was studied. Due to restricted statistics collected, we start with the gate set to $n = 3$, where n is the number of detected neutrons.

The corresponding mass distribution is shown in Figs. 6.26(a) and 6.26(b). A rectangular structure is marked by the arrow. It is observed in the same arm as the bump in Figs. 6.4, 6.23(a). The events forming the rectangle and its vicinity lie in the box $w1$ in the V_1–E_1 distribution presented in the insert. Additional selection with this $w1$ gate reveals the rectangular structure in a more pronounced way (Fig. 6.26b). The rectangle lies well below the line with $M_s = M_1 + M_2 = 252$ amu and it is bounded by the magic isotopes of ^{94}Kr, $^{80-82}$Ge, ^{128,132}Sn, and ^{144}Ba, their masses are marked by the arrows 1–5, respectively.

After the similar procedure for $n = 2$, more events remain and complicated structures appear (Fig. 6.27). A larger concentration of events in the plot appear within the boundaries of masses as marked in the figure (magic isotopes of ^{94}Kr, ^{128}Sn, ^{68}Ni). The extension of the points in the right half of the rectangle likely reflects shell effects around $N = 88$ (neutrons) in the shell correction map [73].

There is negligible background from scattered binary fission fragments in these data, therefore we emphasize the non-random nature of the whole plot. The "tail" of

scattered fragments should look like a smooth curve decreasing monotonically from the locus of conventional binary fission (see, for instance, curve 2 in Fig. 6.23(c)). This is not observed here. The most populated rectangular structure is bounded by magic nuclei, as was mentioned before. The bulk of the points below this structure lie, within mass resolution, only along four discreet directions, namely, M_1 or $M_2 =$ const, $M_1 + M_2 = M_s =$ const (it means that the missing mass is const) and the line to be almost perpendicular to the latter. In order to have an idea of such different structures these possible directions are shown in the lower right corner of the plot for visual comparison with the data. One of the examples of the lines with $M_s =$ const is marked by the number 7, this line corresponds to a missing ^{14}C nucleus.

In order to estimate quantitatively the probability of a random realisation of the lines under discussion, special Monte-Carlo testing was performed using a well known formalism of the Hough transformation [74, 75] for formal revealing of lines consisting of several points. The probability of a random realization of such line does not exceed 2 % (see Appendix for the details) and it is even much lower for a more complicated structure like the rectangle in Fig. 6.26(b).

We emphasize once more that the structures visible in Figs. 6.26 and 6.27 are seen in the same spectrometer arm (and only there) as the bump shown in Fig. 6.23. The rectangular structures have been revealed thanks to neutron gating, which effectively suppressed the background from the scattered FFs of binary fission in the region of interest and selects different CCT-modes. Each event is a true triple coincidence with E-TOF and a group of neutrons. The neutron number is potentially much larger then 3, because of the lower efficiency for neutron detection.

6.6.5.2 Estimation of the CCT Events as a Neutron Source

In our neutron-gated distributions the background due to scattered FFs is negligible, therefore a random generation of linear structures has a low probability. This is important for the interpretation of the structures seen in Figs. 6.26 and 6.27. The structures are the groups of true physical events, and they must be associated with ternary fission events with at least one missing fragment. The fact that the structures appear only with neutron gating means that the neutron source, which produces these events (structures) has parameters, which differ from those of a neutron emission in conventional binary fission.

We try to estimate roughly the neutron multiplicity of the decays for the events shown in Fig. 6.27. Among this matrix 230 events were detected (1.1×10^{-4} per binary fission) in coincidence with two neutrons, and 17 events (8.0×10^{-6} per binary fission) in the same region of the mass correlation plot have the experimental neutron multiplicity three ($n = 3$). We can assume the ternary decay modes to be connected with all the experimental points in Fig. 6.27. The experimental yields for the events $n = 2$ and $n = 3$ are shown in Fig. 6.28 by the triangles.

For further discussion we suppose (model_1): that neutrons are emitted from accelerated fragments moving with the velocities typical for normal binary fission.

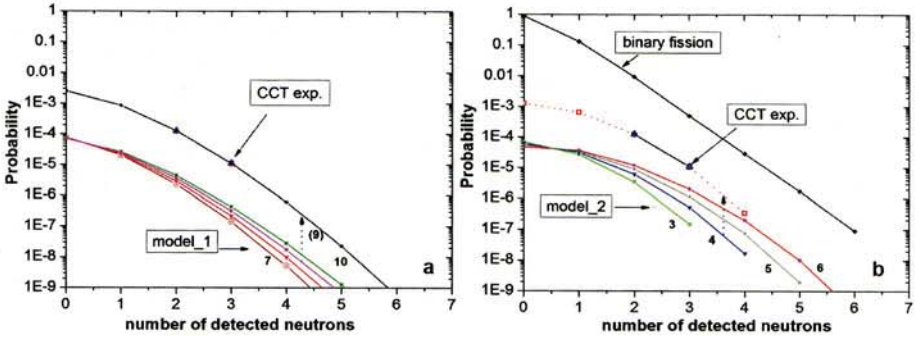

Fig. 6.28 Comparison of the neutron yields associated with CCT (*error bars* do not exceed the dimension of the symbol) with (**a**) the multiplicity spectra for neutrons emitted from the accelerated fission fragments (model_1) and with (**b**) those for isotropic neutron sources (model_2) of different multiplicities (marked near the curves). Each *curve* is normalised arbitrary to the total yield 10^{-4}. The model curves, which provide the best agreement of the slopes with those of the experimental observations are marked by the *arrows*. See text for details

The calculations are based on the model of the neutron registration channel presented earlier in Ref. [64]. Using the slope of the experimental curve as a criterion one can try to choose the best result among the model spectra. We obtain a primary neutron multiplicity of $M\_n = 9$. Very elongated pre-scission shapes are needed in order to provide such increased neutron multiplicity [65]. At the same time we observe the velocities of the detected fragments close to corresponding mean values in normal binary fission. In order to overcome the contradiction the neutron source searched for was supposed to be at rest or isotropic (model_2). The results of modelling the multiplicities of such a situation are compared with the experimental data in Fig. 6.28(b). The best agreement is observed for the slope of the curve corresponding to four neutrons emitted from the experimental centre ($n = 4$).

The results of estimations of the neutron multiplicity obtained in the two different models can be judged as follows: one (model_1) failed to reproduce the experimental data, but it does not exclude that a superposition of two sources (models) exists. It is important that at least a certain part of the detected neutron multiplicity is accounted to a neutron source different from those bound to accelerated fragments. In Refs. [76, 77] and others, an isotropic component is observed in addition to the neutrons emitted from the accelerated fragments. In our case the latter will be detected with a factor 3 lower efficiency.

6.6.5.3 Results of Experiment Ex4

The FFs mass-mass distribution for the events selected with the gates within similar approach as used in Ex3 is shown in Fig. 6.29. Namely, we chose $n = 3$ and a selection with the gate in the V_1–E_1 distribution similar to the box $w1$ in Fig. 6.26(a). Again the rectangular structure is found similar to that seen in Ex3 (Figs. 6.26 and 6.27), however, for a different mass range.

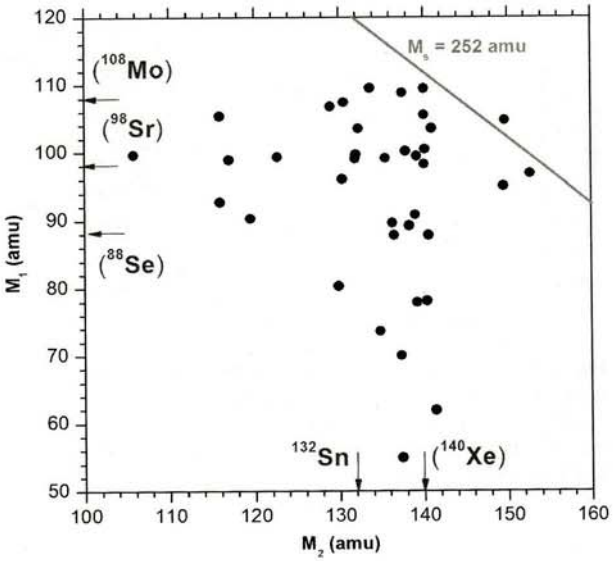

Fig. 6.29 Ex4 ($n = 3$ and $w1$): Results obtained at the COMETA set-up: mass-mass distribution of the FFs from ^{252}Cf (sf) under the condition that three neutrons ($n = 3$) were detected in coincidence and an additional selection with the gate $w1$ in the (V_1–E_1) distribution similar to that shown in Fig. 6.26(a) of Ex3

This structure is invisible in the initial ungated distribution, because it is located very close to the locus of the conventional binary fission events, as can be seen from the comparison of Fig. 6.24 with Fig. 6.29. The additional gates help to reveal new CCT-decay modes with very light fragments, $M_3 = 22$ amu and lighter reaching down to binary fission.

As can be inferred from the figure, the rectangular structure seen in its upper right corner is bounded by the nuclei with the masses in the vicinity of known magic nuclei (shown in the brackets). These masses (except of double magic ^{132}Sn) were calculated based on the unchanged charge density hypothesis for the fission of the ^{252}Cf nucleus. Actually we know that at least three neutrons were emitted in each fission event presented in the figure. A change in the nuclear composition of the mother system can lead to a shift of the masses of the magic nuclei if neutrons were emitted from the decaying system (pre-scission neutrons). Likely this is what we observe here. For the upper right corner of the rectangle both mass and charge conservation laws are met only if the upper side of the rectangle corresponds to the $^{109}_{43}$Tc nucleus while the mass 140 amu corresponds to the isotope composition of $^{140}_{55}$Cs.

The structure manifests itself exclusively thanks to the difference of the neutron sources for the fragments appearing in both binary fission and CCT, respectively. These two decay modes must differ in the neutron multiplicity or/and in their angular distributions of the emitted neutrons in order to provide the higher registration efficiency for neutrons linked with the CCT channel. At the same time the excitation energy of the system at the scission point defined as $Eex = Q - TKE$ (where Q is the reaction energy, TKE—is the total kinetic energy of all the decay fragments), is known from our experimental data. It does not exceed $Eex = 30$ MeV. This value of the excitation energy is high enough to allow for the emission of three or four

neutrons, which corresponds almost to the mean neutron multiplicity of binary fission. Thus the neutron source linked with the new CCT channels must have a much smaller velocity as compared to conventional binary fragments, or it can be almost at rest in the extreme case [17]. The latter agrees with the hypothesis put forward above that we deal with the pre-scission neutrons at least for very light missing masses.

6.6.6 Mass Resolution of the Set-Ups Used

Experiments Ex1, Ex2 and Ex3 were performed using gas filled detectors while PIN-diodes were used in Ex4. The mass resolution achieved in each experiment is discussed separately.

6.6.6.1 Mass Resolution in Ex3

The time-of-flight spectrum of an ^{226}Ra α-source measured at the FOBOS set-up shows a time resolution of 200 ps (irradiating a small central part of the PSAC) and ~400 ps if all the surface of the counter is irradiated (Fig. 4 in [35]). Thus in Ex3 the relative time resolution does not exceed 1 %.

For the energy (E) only the residual energy is measured in the BIC of the FOBOS set-up due to the energy losses in the mylar foils along the flight pass with the total depth of about 1 mg/cm^2. The mass reconstruction procedure was presented in Ref. [39]. The SRIM code [78] allows to calculate the mean residual energy and its variance for the FF after passing of all foils. The relative uncertainty (FWHM) of the measured residual energy does not exceed 2 % and 3 % for typical light and heavy fragments, respectively. Thus the corresponding mass resolutions (within uncertainty of the time-of-flight) are estimated to be approximately 3 amu for the light peak and 4.5 amu for the heavy one.

At the same time the loci of binary fission events (Fig. 6.23(a)) show much worse mass resolution which is ~6 amu and ~8 amu for the typical light and heavy fragments, respectively, even after "cleaning" by gating within condition $P_1 \approx P_2$, where $P_{1,2}$ are the FFs momenta, i.e. momentum conservation law. Such selection allows to exclude the events connected both with random coincidence of FF with alpha-particle and scattered FFs. The estimation of, mass resolution given before (3 amu and 4.5 amu) is related to an ion of a single mass the and a fixed nuclear charge, while actually in the conventional binary fission we deal with the registration of isobaric chains including normally four or five isotopes [79]. At a fixed mass number A the shape of the fractional independent yield $Y(z)$ being non-Gaussian, differs substantially for different FF energies (Table 3 in Ref. [79]). Modeling using the SRIM code shows that the centers of the residual energy spectra for the adjacent isotopes of an isobaric chain are shifted relative to each other by the distance similar or even larger (for heavy fragments) then their width (for instance, ~1 MeV for $A = 110$ amu at the initial energy of $E = 112$ MeV). Such a shift is a decisive factor

for a dramatic increase of the total width of the residual energy spectrum for FFs of fixed mass after passing thick (~1 mg/cm^2) mylar absorber.

It is known as well, that some of the FFs differ essentially by the range and specific energy losses from both the calculated data and the experiments with corresponding unexcited nuclei. A mean value of $q = 3$ charge units was found [80] for the shifted part of the ionic charge state distribution thanks to an Auger cascade linked with the de-excitation of low energy rotational levels.

The procedure of mass reconstruction briefly looks as follows [39]. Let us assume E_{ch} and V_{in} to be the energy of the fragment deposited in the BIC and, respectively, its actual velocity before the BIC entrance. Both are measured in the experiment. The energy E_{cal} of the fragment after crossing of the entrance window of the BIC is calculated applying the table of energy losses [81] for the sequence of masses M_j (in the range 0–250 amu) with the nuclear charge Z_{UCD}, assigned to the corresponding fragment at fixed velocity V_{in}. In order to restore the fragment mass we examine mass-by-mass descending along the calculated dependence on E_{cal} (M, Z_{UCD}, at $V_{in} = \text{const}$) until the following condition is met for the first time: $E_{ch} < E_{cal}$ (M, V_{in}). Strictly speaking such procedure is absolutely correct (within energy and velocity resolution) for the fragment having really $Z = Z_{UCD}$ which does not emit neutrons. The uncertainty due to the neutron emission would shift the calculated charge by some percents only. The uncertainty in the nuclear charge increases the dispersion and distorts the shape of the response function but its most probable value stays unbiased as it was shown in Fig. 3 of Ref. [54].

In Ex3 dispersion of the points along the line number 1 in Fig. 6.27 shows that mass resolution does not exceed 3.5 amu (FWHM). Similar resolution is obtained for $M_1 \sim 94$ amu (the upper side of the rectangle in Fig. 6.26(b)). The value obtained (3.5 amu) is very close to that cited before (3 amu) for typical light binary FFs with fixed nuclear charge. It is reasonable to suppose that the better mass resolution observed, just for the CCT partners as compared to conventional binary fragments, is due to an absence of both factors leading to the mass spread mentioned above, namely, dispersion of nuclear charge at fixed mass and an increased dispersion of the ionic charge due to internal conversion.

From the neutron gated data presented here (see Sect. 6.6.8) we draw the conclusion, that the heavy CCT partners detected are borne rather cold and likely without angular momenta. Some of them have magic nucleon composition providing increased stiffness and stability [73].

6.6.6.2 Mass Resolution in Ex1

In Ex1 MCP based "start" detectors and thinner foils in the gas filled detectors (total thickness of all the foils along the flight path does not exceed 0.6 mg/cm^2) allow a better mass resolution in Ex1 as compared to that in Ex3. For the conventional binary fission events, selected within the condition on the momenta $P_1 \approx P_2$, the mass resolutions are estimated to be 4 amu and 6 amu for the typical light and heavy fragments, respectively.

6.6.6.3 Mass Resolution in Ex4

The time resolution obtained with alpha particles at the COMETA set-up is better than 330 ps [82]. The mean velocity of the Ni-nuclei linked with the lines 2, 3 in Fig. 6.24(a) observed in Ex4 is about 0.75 cm/ns that this gives a relative time resolution of about 2.7 %.

The energy resolution of the semiconductor Si-detectors is mainly defined by the fluctuations of the pulse height defect (PHD). For instance in Ref. [83], the energy resolution of the PIN-diode did not exceeded 1.7 MeV for ^{127}I-ions at the beam energy of 80 MeV. Assuming the energy resolution to be inversely proportional to the PHD value, we can roughly estimate (Fig. 6 in Ref. [83]) for our case the value of 0.25 MeV. Thus the estimated mass resolution does not exceed 2.5 amu. This value agrees well with our data. In Fig. 6.24(b) we show the projection of the linear structure seen in at the masses 68 and 72 amu. The peaks presented and other structures in Fig. 6.24 correspond to the mass resolution of the COMETA set-up to be ~2.0 amu (FWHM).

Due to the rather short flight pass used in the COMETA set-up, the mass resolution is determined mainly by the relative time resolution. For the typical light fragment from binary fission, which is faster and heavier, than a Ni fragment from the CCT process, the mass resolution is calculated to be ~6 amu. It is very close to the estimation obtained from the width of the main locus of fission fragments in Fig. 6.24(a).

6.6.7 Triple Coincidences in Ex4

Another opportunity, namely the observation of slow fragments from the ternary decay as almost isotropic neutron source is confirmed by the other results of Ex4. The individual detectors of the mosaic of the COMETA set-up allow in principle a triple coincidence, i.e. the direct detection of all three partners of a ternary decay. For the sake of convenience the FFs from such events are labelled as m_1, m_2 and m_3 in an order of decreasing masses in each ternary event. Thus designations M_1, M_2 (here m_1, m_2) are different to their previous use. For this case we plot the m_1–m_2 correlation obtained in Ex4 in Fig. 6.30. The rectangular structures in the centre of the figure are bounded by the same isotopes (^{108}Mo, ^{128,132}Sn, ^{140}Xe) or similar (^{110}Tc, ^{102}Zr) magic clusters (their masses are marked by the arrows with the numbers 6, 4, 5, 1, 2, respectively) to those mentioned above in Fig. 6.29. Below the rectangle the horizontal line 3 corresponding to magic ^{98}Sr nucleus is vividly seen. It goes through the thickening of the points 8 centred at the partition of magic deformed nuclei ^{98}Sr/^{142}Xe. The line $M_s = \text{const} = 240$ amu (missing ^{12}C) goes likely through the same point forming the diagonal of the rectangle with the upper left corner at the partition ^{108}Mo/^{132}Sn. The points marked by number 11 lie in the vicinity of the partition corresponding to magic deformed isotopes ^{116}Ru/^{124}Cd

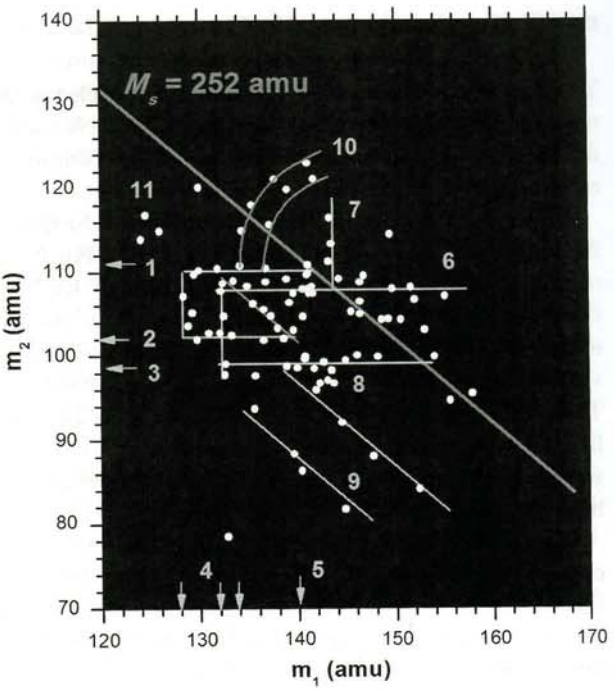

Fig. 6.30 Ex4, but triple coincidences: Mass-mass correlation plot for the two heaviest fragments m_1, m_2 obtained in triple coincidences from ternary decay with the condition $m_1 > m_2 > m_3$ (in an order of decreasing masses of the decay partners, see text). Velocities and energies of the third detected partners (m_3) do not exceed 0.55 cm/ns and 2 MeV, respectively. The *lines* are drawn tentatively to guide the eye. See text for more details

(nuclei from the shell minima C' and K' in Ref. [73]). Lines 8 and 9 correspond to missing masses 16 and 24 amu, respectively.

For these data one more peculiarity of the distribution should be mentioned, namely, now the region where $M_s > 252$ amu becomes populated. A possible explanation is that a heavy fragment formed in the specific decay mode with e.g. ^{108}Mo (line 7) in the exit channel, is followed by a much slower light fragment which, hits the same PIN diode as the previous heavy fragment. The faster fragment defines the TOF. However, the measured energy being the sum of two parts will be incorrect, thus leading to an incorrect evaluation of the mass of the heavy fragment. A similar situation can appear in the case of ^{144}Ba (line 6). Bearing in mind that we really detected three fragments in each event from the distribution in Fig. 6.30 such additional fragment could be the fourth partner of the quaternary decay.

One more remarkable structure consisting of two curves marked by number 10 is connected presumably with a delayed sequential ternary decay. Emission of the light particle provides the "start" signal, and results in a population of a shape isomeric state. Later delayed fission of this isomeric state can occur. Both the heavy fragments formed have distorted (larger) TOFs and, consequently, increased masses.

It should be further mentioned that the velocities and energies of the corresponding lightest central fragments do not exceed 0.55 cm/ns and 2 MeV, respectively. The last number represents also a threshold in the energy channel. Therefore it is not possible to calculate correctly the masses m_3 for the events under discussion.

6.6.7.1 Discussion of Sect. 6.6

With the inclusive data from the new experiments we have confirmed the occurrence of the CCT decay observed previously in Ref. [54]. In the neutron gated data we have observed the new unique rectangular structures bounded by magic clusters in the missing mass data (Figs. 6.26, 6.27). We have seen from the COMETA results (Figs. 6.29, 6.30), that not only spherical (Ni, Ge) but also deformed magic clusters (^{98}Sr, ^{108}Mo) can be the constituents of such structures.

At this stage of the study of CCT-decays we are not ready to propose a detailed physical scenario showing different decay modes and to estimate a scenario for the CCT process in the overall picture of clustering effects in nuclei [84–86]. It means that we may have some questionable assignments in the decay channels of the rare CCT process.

With the new experiments, which have a negligible background in arm2 and in arm1, the yield of events in arm1 (facing the source backing) are true missing mass events (each event is a true coincidence). Additional selection of CCT events in this region has been achieved by the selection with a gate in the V–E space, and, in addition, with the experimental neutron multiplicities, which implies $Y_{exp\_CCT}(n) \gg Y_{bin}(n)$ in some region of the missing mass space. The neutron source is indeed connected to the ternary fission mode with different mass partitions. Keeping in mind the results of Sect. 6.6.5.3 and 6.6.7, we may assume two different sources of neutrons emitted almost isotropically, namely, from the decaying system before scission (pre-scission neutrons) and from the slow middle fragments of ternary decay. The emission of pre-scission neutrons from the primary nucleus from a strongly deformed shape can be taken as a signature of a complicated fission process.

It has already been stressed, that revealing the CCT mode by means of neutron gating is possible only if the neutron sources connected to the CCT and conventional binary fission, respectively, differ by neutron multiplicity or/and their spatial distribution of the neutrons. The latter can enhance the CCT registration probability due to the geometry of the neutron detectors assembly (neutron belt) used (Figs. 6.20, and 6.21). Possible differences in the neutron energy spectra are not important, because we have experimental evidence that two layers of neutron counters in the moderator are enough for the registration of fission neutrons hitting the neutron belt.

Thus we have observed the rectangular structures seen in Figs. 6.26, 6.27, and 6.29 due to the fact that with the specific neutron assembly used, the probability $Y_{bin}(n)$ decreases (Fig. 6.25) with the increase of neutron multiplicity (n) in the corresponding region of the mass correlation plot.

Further comments are needed for the evident difference in the structures seen in Figs. 6.26 and 6.29, respectively, while a similar additional selection gate $n = 3$ was used in both cases. We know (Sect. 6.6.4.3) that the yield $Y_{phys} \times P_{miss}$ is approximately four times smaller at the COMETA set-up as that at the modified FOBOS spectrometer. At the same time both set-ups have very similar values of P_n (Sects. 6.6.1 and 6.6.2), i.e. $Y_{exp\_CCT}(n)$ (formula (3)) was less in Ex4 in general. Keeping in mind that the experimental yield of the different "bumps" increases

considerably from the "Ni"-bump to "Mo"-bump [87] it is understandable why we see only "Mo"-bump in Ex4 in the neutron gated data. According to the logic presented, the "Mo"-bump must be seen as well in Ex3 within $n = 3$ gate. This is really so, however, we do not show this part in Fig. 6.26(b) (is above the rectangle), because a complicated superposition of different structures observed there. Additional structures as compared to Ex4 are due to the difference in the blocking mediums in these two experiments.

We comment also on the opening angle of the CCT events and the probability of their registration. We need an opening angle between the two fragments to detect them. Its major part comes from multiple scattering in the backing (and eventually foils) [78]. The originally collinear fragments can have also a primary (intrinsic) angular divergence. That this value is negligibly small can be deduced from the recently discovered ROT effect [88]. The phenomenon is traced to the rotation of the fissioning nucleus while light particles are ejected. The effect has been observed for the first time in fission of the ^{235}U nucleus induced by cold polarized neutrons. After capture of a polarized cold s-neutron, the ^{236}U* nucleus has the possibility of two spin states 3 and 4, corresponding to two opposite senses of rotation. It was discovered that the angle through which the fission axis rotates with respect to the trajectories of α-particles from conventional ternary fission, is very small and barely exceeds 0.2°. This takes place because the rotation after scission is very short-lived and comes to a virtual stop after some 10^{-21} s due to the drastic increase of the moment of inertia of the system consisting of two fragments flying apart. Thus, even if a di-nuclear system consisting of two CCT partners has an angular momentum of some units of $\hbar$, it is reasonable to expect a situation comparable with the ROT effect, a negligible angular shift between the fission axis of the initial system and that of the di-nuclear system formed after the first rupture.

In general the CCT-decay is most likely due to a sequential process with two scissions in a short time sequence. As was shown in Ref. [54] the three body chain-like pre-scission configuration which can lead to the CCT in the frame of such sequential process, is linked with the slopes in the potential energy valley of the decaying system. Evidently this fact explains the much lower yield of the CCT as compared to binary fission which is realized via shapes corresponding to the bottom of the same potential valley. The overall relative yield of 3×10^{-3} contains a large number of mass combinations, as well the enlarged phase space due to higher Q-values and the excited states of the fragments [17].

6.6.8 Conclusions to Sect. 6.6

We have performed studies of fission-decays of ^{252}Cf with coincidences of the emitted neutrons in two missing mass experiments Ex3 and Ex4. These experiments confirm the observations of the ternary fission process as collinear cluster tri-partition (CCT), which has been observed in previous experiments (Ex1), described in Ref. [54]. The results give new information on the different CCT decay modes (mass partitions):

- The bump discussed earlier in Ex1, Ref. [54] does not show a unique combination of ternary masses. Bearing in mind the results presented in Figs. 6.24, 6.26(b), 6.27, 6.29, and 6.30, we observe a sequence of mass partitions. Most structures are based on pairs of magic nuclei, combined with isotopes like ^{128,132}Sn.
- Specific linear and rectangular structures are observed in Ex3 and Ex4 with increasing neutron multiplicity (shown in Figs. 6.26(b), 6.27, 6.29). This observation was possible, thanks to a very low background provided by the neutron gating or using mosaics of PIN diodes (with no material in the path of the fragments) in Ex4. These structures provide unique information concerning the evolution of the decaying system near the scission point. Only in this case one can analyse CCT in the multidimensional $\{M_1, M_2, V_1, V_2, E_1, E_2\}$ space event by event. In fact, such analysis is impossible in principle for Ex1 with the high background from scattered binary fission events (subtracted by showing the differences of (arm1–arm2)). These events are within the bump observed in Fig. 6.4. The "background" contains also a sum of different CCT-modes, and as a whole the sum of CCT components is statistically very significant in the absolute scale.
- It should be emphasized that the yields of the "Ni"-bump ($\sim 4 \times 10^{-3}$/binaryFF) and even at heavier masses for the "Mo"-bump [87] ($\sim 10^{-2}$ per binary fission), are attributed to some tens of different partitions forming in fact the corresponding bump. As was mentioned above the yield of a fixed partition, for instance, ^{68}Ni/^{128}Sn (Fig. 6.24) does no exceed $\sim 10^{-5}$/binary fission. Just this yield can reasonably be compared to the probability of known conventional ternary decays with a single light mass isotope emitted.

6.7 Experiments on the Heavy Ion Beams

6.7.1 *Collinear Multi-Body Decays in the Reaction* ^{238}U + ^{4}He *(40 MeV)*

Direct detection of all decay partners is desirable for reliable identification of unusual reaction channels, e.g. a spectrometer of high granularity should be used. Such one installed at JYFL (Jyväskylä, Finland) was chosen for studying the reaction ^{238}U + ^{4}He (40 MeV) by the international team taking part in HENDES and FOBOS collaborations. The experimental set-up (Fig. 6.31) was assembled as double-arm TOF-E (time-of-flight vs. energy) spectrometer with micro-channel plate (MCP) detectors and mosaics of 19 PIN diodes each. Altogether, about 40 millions binary fission events were collected. Besides binary ones, the ternary and quaternary coincidences were also detected in the experiment. Experimental method and data processing are presented in more detail in Refs. [89, 90]. What should be especially mentioned is that fission fragments (FF) mass resolution achieved in the frame of the velocity-energy method does not exceed 2.5 amu (FWHM).

We discuss here only events with the multiplicity three what means that three fragments were detected in coincidence. By convention, M_a denotes below the heaviest mass, M_b—the middle one, and M_c—the lightest fragment mass in the triplet.

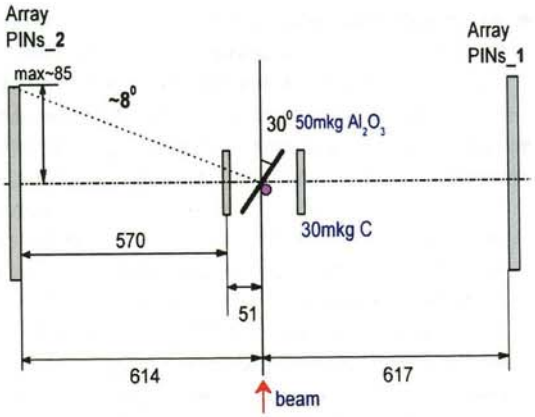

Fig. 6.31 Scheme of the experimental set-up for $^{238}U + ^{4}He$ (40 MeV) measurements. All distances are shown in millimeters

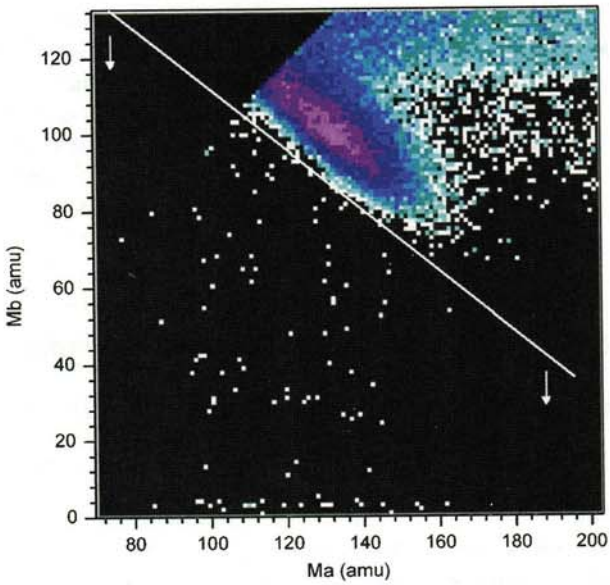

Fig. 6.32 Ternary events under analysis. See text for details

The events under analysis are shown in Fig. 6.32 the white line. The locus and a tail above this line are due to random coincidences. The events with the mass M_b less than 8 amu are also beyond the scope of this report as they were already discussed in our previous publications [91, 92].

It is reasonable to start from the events where a total mass of the detected fragments is equal to the mass of the compound system within the experimental mass resolution. In the following three events the magic or double magic Sn nuclei were detected as the heaviest fragments Table 6.1.

Corresponding light fragment (deformed magic nucleus) was clusterised in the scission point forming dinuclear system. Its brake-up appears to occur due to inelas-

Table 6.1 Mass conservation law is met in the events presented

Point number	Decay scheme
1	$^{128}\mathrm{Sn}+{}^{32}\mathrm{Mg}+{}^{80}\mathrm{Ge}+\mathbf{2n}$ → $^{112}\mathrm{Ru}$
2	$^{132}\mathrm{Sn}+{}^{68}\mathrm{Ni}+{}^{42}\mathrm{S}$ → $^{110}\mathrm{Ru}$
3	$^{130}\mathrm{Sn}+{}^{72}\mathrm{Ni}+{}^{40}\mathrm{S}$ → $^{112}\mathrm{Ru}$

Table 6.2 Dinuclear molecules based on deformed magic constituents

Point number	Decay scheme		Point number	Decay scheme	
1	$^{121}\mathrm{Ag}+{}^{23}\mathrm{F}+{}^{65}\mathbf{Mn}+{}^{33}\mathrm{Al}$		4	$^{140}\mathrm{Xe}+{}^{25}\mathrm{Ne}+{}^{62}\mathbf{Cr}+{}^{15}\mathrm{C}$	
	$^{144}\mathrm{Ba}$	$^{98}\mathrm{Sr}$		$^{165}\mathrm{Gd}$	$^{77}\mathrm{Zn}$
2	$^{113}\mathrm{Ru}+{}^{31}\mathbf{Mg}+{}^{78}\mathrm{Ni}+{}^{20}\mathrm{Ne}$		5	$^{134}\mathrm{Te}+{}^{30}\mathbf{Ne}+{}^{50}\mathrm{Ca}+{}^{27}\mathrm{Ne}+\mathbf{n}$	
	$^{144}\mathrm{Ba}$	$^{98}\mathrm{Sr}$		$^{164}\mathrm{Gd}$	$^{77}\mathrm{Zn}$
3	$^{130}\mathrm{Sn}+{}^{14}\mathbf{C}+{}^{62}\mathrm{Cr}+{}^{33}\mathrm{Mg}+\mathbf{3n}$		6	$^{110}\mathrm{Tc}+{}^{11}\mathrm{Be}+{}^{62}\mathrm{Cr}+{}^{58}\mathbf{V}$	
	$^{144}\mathrm{Ba}$	$^{95}\mathrm{Rb}$		$^{121}\mathrm{Ag}$	$^{121}\mathrm{Ag}$

tic scattering on the material of the start-detector. Such hypotheses is based on the fact that a momentum conservation law is not met in all three events.

In the next set of events the decaying system was also fully clusterised i.e. its mass was exhausted by two magic constituents. Both "initial" clusters undergo fragmentation leading to formation of two dinuclear molecules. In contrast with previous case both "initial" clusters are relatively soft deformed nuclei. Some examples of the events under discussion are presented in Tables 6.2 and 6.3.

The last group combines the events where initial system looks like a chain of three magic clusters. The middle cluster is clusterised in its turn in such a way that one of the constituent shows as well magic nucleon composition. Typical events are shown below in Table 6.3.

Two of them (No. 1, 4) are absolutely identical. It is hard to believe that such astonishing reproducibility could be due to the random coincidences. A presumable scenario which stands behind these events is illustrated by Fig. 6.33.

One sensitive point of the methodic used should be mentioned before coming to the conclusions. As it is shown in Fig. 6.31 the "start" detectors are located at some distance from the target because evidently they can not work properly right

Table 6.3 Three-body molecules based on magic constituents

Point number	Decay scheme	Point number	Decay scheme
1	$^{98}Sr + {}^{42}S + {}^{28}Mg + {}^{72}\mathbf{Ni} + \mathbf{2n}$	5	$^{120}Pd + {}^{32}Mg + {}^{18}O + {}^{72}\mathbf{Ni}$
	missed		
	^{70}Ni		^{50}Ca
2	$^{108}Mo + {}^{40}S + {}^{18}N + {}^{72}\mathbf{Ni} + \mathbf{4n}$	6	$^{95}Rb + {}^{42}S + {}^{22}F + {}^{82}\mathbf{Ge} + \mathbf{n}$
	^{58}V		^{65}Mn
3	$^{84}Se + {}^{52}Ca + {}^{30}Mg + {}^{72}\mathbf{Ni} + \mathbf{4n}$	7	$^{142}Xe + {}^{34}Al + {}^{14}N + {}^{52}\mathbf{Ca}$
	^{82}Ge		^{48}Ca
4	$^{98}Sr + {}^{42}S + {}^{28}Mg + {}^{72}\mathbf{Ni} + \mathbf{2n}$	8	$^{126}In + {}^{30}Mg + {}^{20}O + {}^{66}\mathbf{Mn} + \mathbf{n}$
	^{70}Ni		^{50}Ca

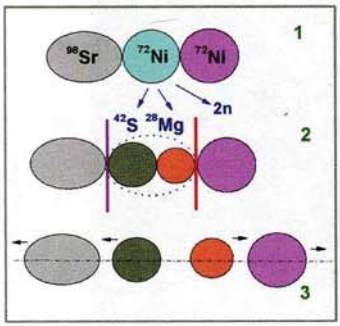

Fig. 6.33 Presumable scenario of one mode of collinear multi-body decay

in the beam. Such geometry, forcedly used, is decisive for some uncertainties in determining of the fragments' velocities, namely, only faster from two fragments which sequentially hits the same start detector shows correct velocity. We discussed this point in detail in Refs. [89, 90].

6.7.1.1 Conclusions

- Treating of the ternary events from the reaction $^{238}U + {}^{4}He$ (40 MeV) proposed is based on the hypothesis that proper i.e. unshifted velocity values were measured. It is hard to believe that stable and strong correlations observed in decay schemes might be due to random coincidences.
- In the frame of such approach two modes of collinear multi-body decay of $^{242}Pu^*$ were revealed. The yield of unusual events (low limit) is about 10^{-6}/binary fission. Pre-scission shape of the decaying system looks like a chain consisting of two or three magic clusters respectively.

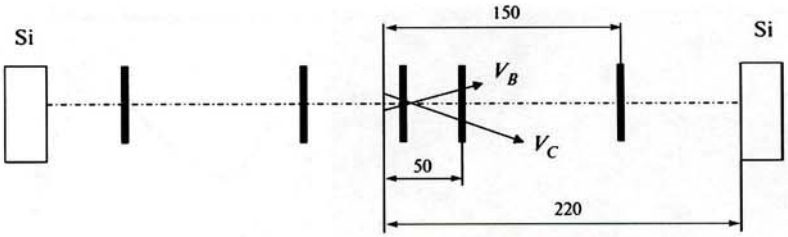

Fig. 6.34 Scheme of the experimental setup for ^{232}Th + d (10 MeV) measurements. See text for details

- Formation of long lived "nuclear molecules" (or isomers) based on magic nucleus and light cluster can appear to occur in the scission point.
- Disintegration of such molecule comes from inelastic scattering on the target backing or "start" detector.
- We estimate our results as strong indication of new effect. Bearing in mind principal uncertainties in velocity measurements at HI-beam mentioned above, improved experimental methods are needed in order to exhaust the problem in forthcoming experiments.

6.7.2 CCT in ^{232}Th + d (10 MeV) Reaction

6.7.2.1 Experiment and Results

For better understanding of the effect revealed the programme of studying of its manifestations in different nuclear systems in a wide range of excitations was adopted. From the methodical point of view direct detection of all decay partners proves to be more convincing experimental approach reference to "missing mass" method used earlier. Thus much more complicated spectrometer of high granularity is needed. Experimental facility of such kind was used for searching for CCT channel in the reaction ^{232}Th + d (10 MeV) (Fig. 6.34) [93]. The experiment was performed by the collaboration FLNR (JINR)–ATOMKI (Hungary). Two microchannel (MCP) based timing detectors and mosaic of nine 2 × 2 cm^2 Si surface-barrier semiconductor detectors in each spectrometer arm were used in order to measure fragments masses in the frame of both the double-velocity and velocity-energy methods. Each Si detector delivered both energy and timing "stop" signals in the events discussed below while "start" signal was taken from the timing detector located at 170 mm from the mosaic. About 5.5 × 10^6 fission events were analyzed all in all.

Two different approaches were used for calibration of time-of-flight (TOF) and FF energy. More simple and rough one looks like as follows. Known FF velocity spectrum for ^{252}Cf (sf) was used for calculating the two coefficients in the linear TOF calibration function. Energy losses in the source backing and timing detectors

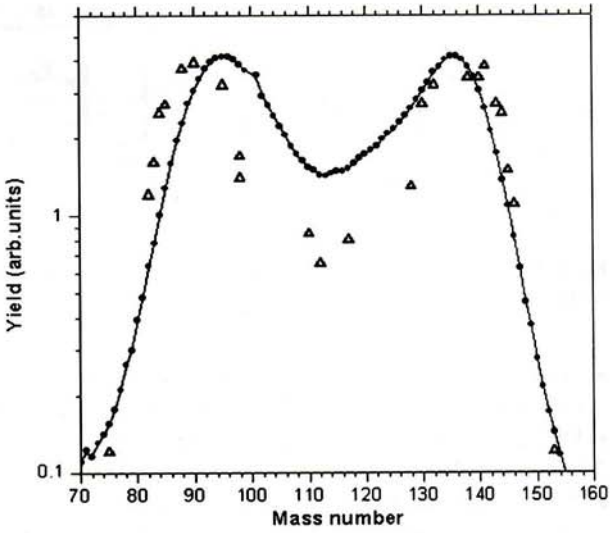

Fig. 6.35 Comparison of the M_{TE} spectra obtained in this work (*circles*) and M_{TE} spectra from the reaction $^{232}\mathrm{Th} + d$ (11.5 MeV) [94] (*triangles*). The latter was obtained by radio-chemical method

foils were ignored. In order to determine parabolic calibration dependence "channel-energy" the known positions of the peaks in the double humped energy spectrum of the FF for $^{252}\mathrm{Cf}$ (sf) and the peak for alphas were exploited. This approach is called below as "3-point" calibration. Resultant spectrum of the FF M_{TE} masses (velocity-energy method) summed over all Si detectors is shown in Fig. 6.35.

As can be referred from the figure both mass peaks of the light (L) and heavy (H) fragments in the spectrum obtained in our experiment are shifted to the center, but so that $\langle M_L \rangle + \langle M_H \rangle \approx 230$ amu what gives approximately correct post-neutron total mass of fragments.

The second calibration procedure used is based on parameterization of pulse height defect in Si surface-barrier detectors proposed in Ref. [61]. Energy losses of the FF over the flight path are also taken into account. Unknown calibration parameters are calculated by fitting of the experimental M_{TE} quasimass spectrum to the known one for $^{252}\mathrm{Cf}$ (sf) [90]. Unfortunately, the quality of the Si-diodes let us to exploit them in the run only at relatively low voltage.

Likely this is the reason for overestimated mass values obtained for $^{234}\mathrm{Pa}^*$ (approximately six mass units on total mass) while the FF M_{TE} spectrum for $^{252}\mathrm{Cf}$ (sf) is reproduced well.

All ternary events analyzed below were calibrated in the frame of "3–point" approach. For the sake of convenience the fragments in each ternary event were re-sorted in order of decreasing of fragment mass, namely, M_1 to be the heaviest, M_2 is a middle one and M_3 is a lightest. Ternary events detected are shown in Fig. 6.36. Their total yield is about 1.6×10^{-5} per binary fission. A bulk of points in the figure lie above the line $M_s = M_1 + M_2 = 234$ amu, i.e. the mass of the compound nucleus. As was shown earlier [90], the measured velocity of the less rapid fragment from the pair of those flying in one direction (Fig. 6.34) will be shifted due to the fact that the faster one gives the "start" signal. This shift in the velocity results in

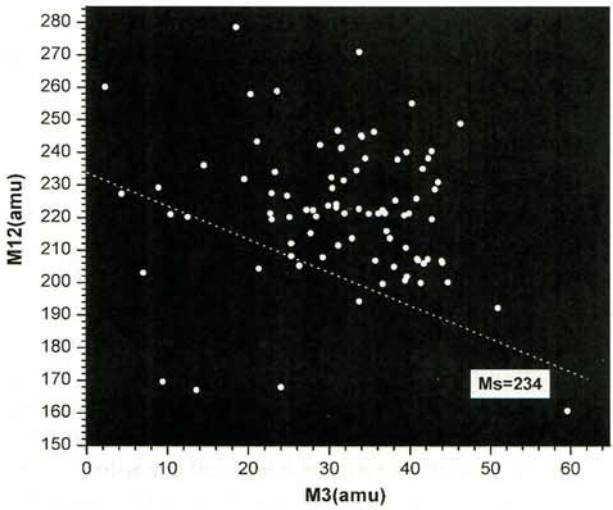

Fig. 6.36 Ternary events detected in the reaction $^{232}\mathrm{Th} + d$ (10 MeV). Here $M_{12} = M_1 + M_2$

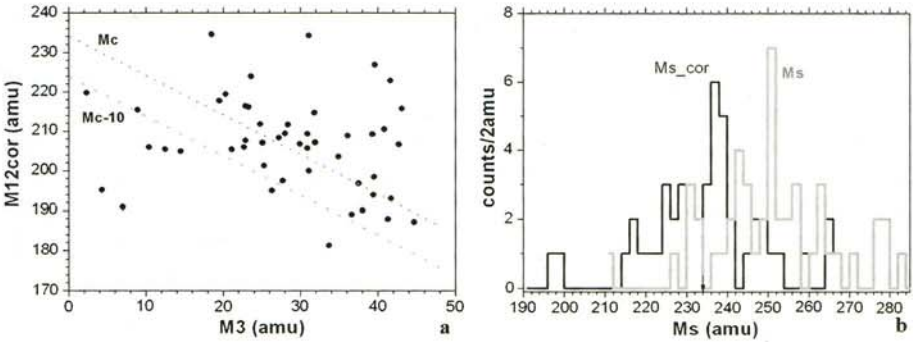

Fig. 6.37 Scatter plot of ternary events after correction of mass M_1—(**a**). The *upper tilted line* corresponds to the mass M_c of the compound nucleus. Comparison of the spectra of total masses of ternary decay products: initial one (M_s) and corrected (M_{s_cor})—(**b**). The mass of compound nucleus is marked by the *arrow*

too high corresponding mass value. Thus the events lying above the tilted line in Fig. 6.36 could be due to this effect. The proper velocity V_{emis} of slower fragment B having experimental velocity V_{exp} can be calculated according to the formula:

$$V_B^{emis} = \frac{22}{(\frac{17}{V_B^{exp}} + \frac{5}{V_C})}, \tag{6.4}$$

where V_C is the velocity of the faster partner in the pair.

In all ternary events where the decay partners with the masses M_1 and M_3 fly in one direction we observe positive difference V_3–V_1. The scatter plot of these events after correction of the mass M_1 (the slower fragment) is presented in Fig. 6.37(a). Figure 6.37(b) demonstrates the difference in spectrum of total mass before and

after correction, respectively. Position of the main peak in the corrected spectrum is a little bit shifted, namely, $M_{s\_cor} = 237$ amu. It could be connected with the fact that experimental velocities were used for calculations within formula (6.4) instead of unknown proper velocity values which have the fragments on the flight path "target-start detector" (Fig. 6.34).

A "shoulder" of main peak from the left side (Fig. 6.37(b)) is likely due to missing of forth fragment of mass ~10 amu (see the bottom line in Fig. 6.37(a).

Similar procedure of mass correction was applied to ternary events where the fragments of ranks "2" and "3" fly in the same direction (approximately half of all events). All of them show overestimated total mass values even after correction. We suppose a following scenario lies behind. Di-nuclear system (molecule) formed after scission of the initial nucleus knocks out ^{12}C ion from the target backing. At the same time this inelastic scattering destroys the molecule. As a result three ions fly in the same direction and ^{12}C ion is the fastest among them. Thus, both V_3 and V_2 velocities must be corrected according to the formula (6.4) what leads to increasing corresponding masses M_3 and M_2. Quantitative testing convinced us that such scenario is absolutely realistic. Unfortunately, true energy of the scattered ^{12}C ion is unknown in each event under analysis preventing one from making proper correction.

The mass spectrum $Y(M_3)$ of the lightest fragments in each detected triplet of fragments under condition $M_s < 242$ amu, which is the right border of the main peak in spectrum of M_{s_cor} in Fig. 6.37(b), is shown in Fig. 6.38(a). Similar spectrum for all ternary events detected is presented in Fig. 6.38(b). Comparing the spectra one comes to conclusion that the latter could be transformed to the first one by "swapping" the counts from heavier to lighter masses. It is precisely the tendency predicted by the scenario above linked with knockout of fast ^{12}C ions.

6.7.2.2 Discussion

In the previous sections the island of high yields of the CCT events (two-dimensional bump) in the mass-mass distribution of the FF from ^{252}Cf (sf) and ^{235}U(n_{th}, f) are discussed. In both cases the bump shows the same internal structure consisting of the ridges $M_s = \text{const}$. While the masses of initial decaying systems differ by 16 amu, positions of the ridges stay in the range (200–212) amu. We supposed that the pairs of magic nuclei (light plus heavy one) of Ni, Ge and Sn stand behind this permanency. Here we observe directly the light fragments calculated in the cited works as "missing" masses amended the total masses of the pairs of magic clusters resulted in the mass of the mother system. It seems quite clear which physics rules the effect. As in well known heavy ion radioactivity (cluster decay) the double magic Pb cluster plays a key role, a pair of magic clusters does the same in the CCT mode under discussion.

The idea put forward is confirmed as well by the results obtained by M.L. Muga and coworkers [95]. Mass spectra obtained in this work for the lightest fragment published by M.L. Muga are compared in Fig. 6.39.

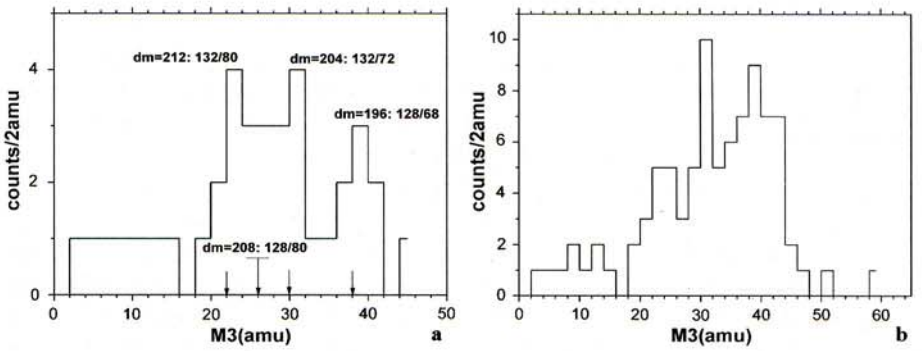

Fig. 6.38 Mass spectrum of the lightest fragments in each detected triplet of fragments under condition $M_s < 242$ amu (see Fig. 6.37(b))—(**a**). Similar spectrum for all ternary events detected—(**b**). The *arrows* in the figure mark the partitions based on pairs of known magic nuclei of Ni, Ge, Sn

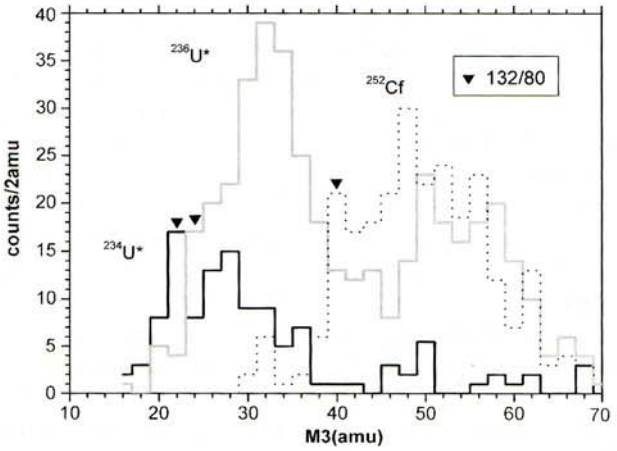

Fig. 6.39 Mass spectra of lightest fragment in ternary fission of three different fissioning systems [95]. *Triangles* are mark the partitions corresponding to the fixed difference $M_c - M_3 = 212$ amu presumably linked with total mass of magic clusters of ^{132}Sn and ^{80}Ge

As can be judged from the figure the confines of the gross peaks in the spectrum for ^{234}U* and this shown in Fig. 6.38(b) are in good agreement. We observe as well the tendency similar to this revealed in our previous data, namely, gross peak in the mass spectrum of the lightest fragments changes its position following the mass of compound nucleus. Really, the sharp rise of the yield in all three spectra presented in Fig. 6.38 starts at the partitions (marked by the triangles) corresponded to the same value of difference $M_c - M_3 = 212$ amu presumably linked with total mass of magic clusters of ^{132}Sn and ^{80}Ge.

Ternary decays were detected in Ref. [89] by three Si semiconductor detectors placed at 120° to each other. Estimated yield did not exceed 10^{-6}/binary fission. The effect for the ^{234}Pa* is observed in our measurements at the level of 10^{-5}/binary fission, but these values can be hardly compared due to absolutely different geometry of the experiments. Total angular distribution of the ternary decay partners is also

unknown for the moment. We can only remind that in the events identified as ternary decays in the frame of the missing mass approach the two detected fragments fly in the opposite directions (i.e. at 180° to each other) within the angular resolution to be less then 2°. An experimental angular spread of the fragments originated from the ternary decay of ^{234}Pa* flying in one direction can range from 1° up to 20°. Thus measuring both angular distribution of partners of ternary decay under discussion and its yield stays an actual goal of special forthcoming experiments.

Due to peculiarities of the FF energy calibration used we lack opportunity to analyze accurately mass-energy correlations of ternary decay products in the wide range of masses and energies. By its nature the calibration works well only in the vicinity of three points on the *E–M* plane chosen as reference points. Just imperfection of the calibration forces us to treat the results as "preliminary".

6.7.2.3 Conclusions

Basing on direct detection of three coincident reaction products we declare first observation of true ternary fission of ^{234}Pa* from the reaction ^{232}Th + d (10 MeV). The yield of the effect being dependent from the geometry of the experiment is about 10^{-5} per binary fission. Experimental angular spread of the ternary decay products flying in one direction can range from 1° up to 20°. Mass spectrum of the lightest fragments in each detected triplet of fragments shows gross peak in the range of (20–40) amu. The spectrum agrees with this followed from our previous experiments aimed at searching for collinear ternary decays performed in the frame of missing mass approach. It is in good agreement as well with the similar spectrum obtained by Muga et al. for ^{234}U* [95].

Available data confirm our hypotheses put forward earlier that the lightest among the ternary decay partners amends the total mass of pair of magic clusters Ni/Sn or Ge/Sn forming magic "core" up to the total mass of fissioning system. It is reasonable to suppose that as in heavy ion radioactivity (cluster decay) the double magic Pb cluster plays a key role, pair of magic clusters does the same in the CCT mode under discussion. A decisive role of magic pairs of Ni/Sn and Ge/Sn in ternary decay seems to be expectable bearing in mind that they govern in the conventional binary fission as well [96–99].

6.8 Clustering in Binary and Ternary Fission—Comparative Analysis

An exceptional role of the shell effects in fission of low excited nuclei is a well-known thesis of the fission theory. The first attempts to create the model of the fission process involving shell aspect were taking place in early fifties of the last century. V.V. Vladimirski [100] was maybe the first who postulated that fission probability has noticeable value only if two cluster structures such as magic cores within the

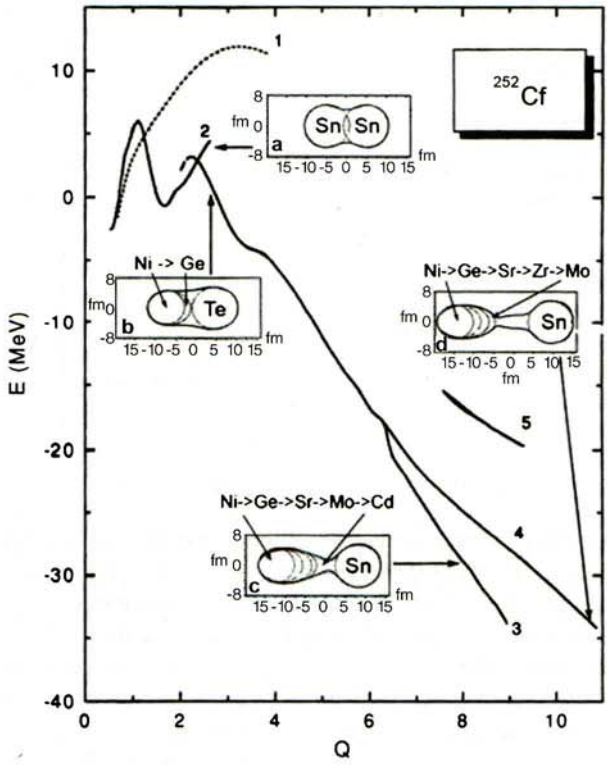

Fig. 6.40 Potential energy of the fissioning nucleus ^{252}Cf corresponding to the bottoms of the potential valleys, as a function of Q, proportional to its quadrupole moment. The valleys are marked by numbers *1* to *4*. The panels depict the shapes of the fissioning system at the points marked by *arrows*

light and heavy fragment corresponding to the $N = 50$ and $Z = 50$, $N = 82$ shells are not destroyed. A dumbbell-like configuration consisting of two magic clusters connected by a flat cylindrical neck was considered as a typical shape of the fissioning system.

The hypothesis put forward in the past was confirmed for the ^{252}Cf nucleus by the calculations carried out in Ref. [97] by the Strutinsky method with the Woods-Saxon potential. The nuclear shape was parameterized in the coordinate system based on Cassini ovals. Minimizing the potential energy with respect to the deformation parameters α_1–α_{10} one obtains potential energy surface (PES) as a function of elongation and mass asymmetry parameters. The resultant PES shows several separate valleys (Fig. 6.40). In each valley the shape of fissioning system is determined by two geometrically invariable constituents which are close to the magic spherical or deformed nuclei in composition and shape and they are called clusters. The formation of di-cluster configurations of the fissioning system appears to be a crucial factor leading to the multi-valley structure of the PES and to the fission modes which the valleys give rise to. The results obtained provide reliable evidence for the di-cluster mechanism of forming the fission mode, proposed earlier in Ref. [101].

Calculations also based on the Woods-Saxon-Strutinsky model involving many deformation degrees of freedom let one show that the density distribution at the third minimum of the fission barriers of the actinides looks like a di-nucleus. It consists of

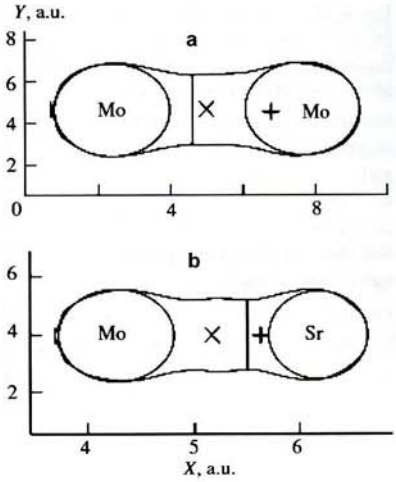

Fig. 6.41 The shape of the nucleus at the bottom of the "symmetric" valley ($Q_2 = 7.52$ a.u., $\eta = 0.074$) (**a**); the same system at the point $Q_2 = 7.52$ a.u., $\eta = 0.208$ (**b**). See text for details

nearly-spherical heavier fragment (around double magic ^{132}Sn) and well-deformed lighter fragment (from the neutron-rich $A \sim 100$ region) [102].

An image of the most populated fission modes in the measured M-TKE (mass-total kinetic energy) distribution was visualized in Ref. [99]. A typical image looks like a trajectory which connects two magic clusters, for instance, ^{132}Sn and ^{80}Ge.

Studying super-asymmetric fission the authors of [98] also came to conclusion that a fine structure in the FFs yields at $A = 70$ ($Z = 28$) seen in all analyzed reactions shows that fission is not only determined by the double shell closure in the heavy sphere of the scission point dumbbell configuration around $A = 132$ ($Z = 50$, $N \approx 82$) but also by an effect of the double shell closure of $Z = 28$ and $N \approx 50$ in the corresponding light sphere. Manifestation of the proton shell effect for the mass $A = 70$ at nuclear charge $Z = 28$ was noted in both neutron and proton induced fission of actinides [46, 103].

Direct indication on a deep link between binary fission and CCT was obtained in our work [33]. The elongated prolate configuration with two necks for the fissioning ^{252}Cf nucleus was demonstrated. This result was obtained in more detailed calculations of the potential energy surface of the ^{252}Cf nucleus carried out in the framework of the procedure presented in Refs. [97, 104] based on the Strutinsky method. Fig. 6.41 depicts the shape of the fissioning nucleus at the bottom of the "symmetry" valley with the quadrupole moment $Q_2 = 7.52$ a.u. The system that fissions in the vicinity of the bottom of the potential valley constitutes two magic nuclei (clusters) connected by a neck. In Fig. 6.41(a), these clusters are the deformed magic nuclei of ^{108}Mo ($\beta_2 \sim 0.58$). In the calculations, the shape of the system was varied in such a way that the value of Q_2 remained constant while the mass-asymmetry η changed starting from the value corresponding to the valley's bottom. By definition, $\eta = (M_1 - M_2)/M_c$, where $M_{1,2}$ is the mass of the system concentrated, respectively, on the left and on the right sides of the varied boundary, which divides the nuclear body into two parts (marked by vertical lines in Fig. 6.41), and Mc is the mass of the fissioning nucleus. As a result, the new shape of the system shown in Fig. 6.41(b)

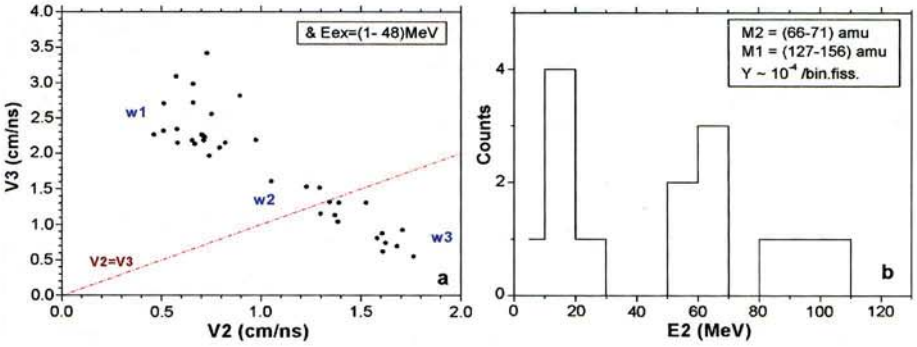

Fig. 6.42 (**a**) The velocities for the lightest (V_3) vs middle-mass (V_2) fragments from the ternary decay. (**b**) The energy spectrum of the Ni fragments from the events of the group $w2$ in (**a**)

was revealed for the first time. The energy of the system is only slightly higher (by ~2 MeV) than the corresponding value at the bottom. The distinguishing feature of the shape observed is the double waist which vividly divides the system into three parts of comparable masses namely clusters of $^{108}Mo_{66}$, $^{98}S_{38}$, $^{46}Ar_{28}$. Magic numbers are marked at the bottom of the element symbol. Thus, all three constituents are the magic nuclei. It would appear reasonable to identify the double rupture of such a configuration as true ternary fission (ternary cluster decay).

Thus, the pre-formation of two magic constituents in the body of the elongating fissioning system can be considered as an established fact. Just different pairs of magic clusters give rise to the different fission modes being the key feature of a low energy binary fission. It is reasonable to expect that clusterisation of the nucleons of the "neck" connecting two magic clusters could lead to forming of multi-body chain-like pre-scission configurations. The latter provides multi-body fission and CCT as one of the possible modes of such process.

6.9 Perspectives

Our plans on further studying of the CCT process are based on first results of quantitative treatment of the experimental data obtained so far. For instance, the events forming the line $M_1 \approx 68$ amu in the mass correlation plot (Fig. 6.24) were analyzed [105]. The mass and velocity of a "missed" fragment were calculated basing on the mass and momentum conservation laws.

Figure 6.42(a) demonstrates the correlation between the velocities of the two lighter partners of the ternary decay. The FFs from ternary events are labeled by numbers 1–3 in decreasing sequence of their masses. Three different groups of the events are vividly seen in the figure. They are marked by the signs $w1$–$w3$, respectively. The events in each group were analyzed separately. The energy spectrum of the detected Ni ions is shown in Fig. 6.42(b). Their yield does not exceed 10^{-4} per binary fission.

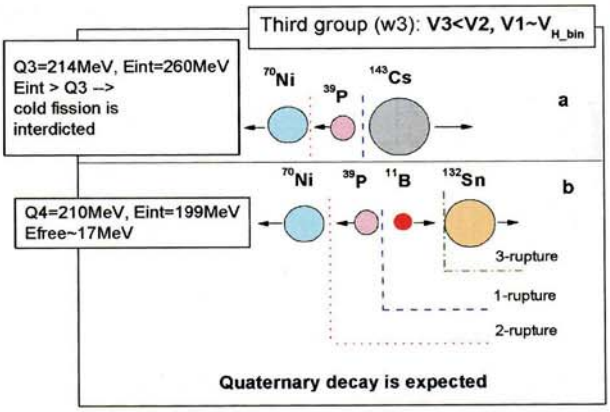

Fig. 6.43 (**a**) The parameters of the events from group *w*3. (**b**) The possible pre-scission quaternary configuration for these events

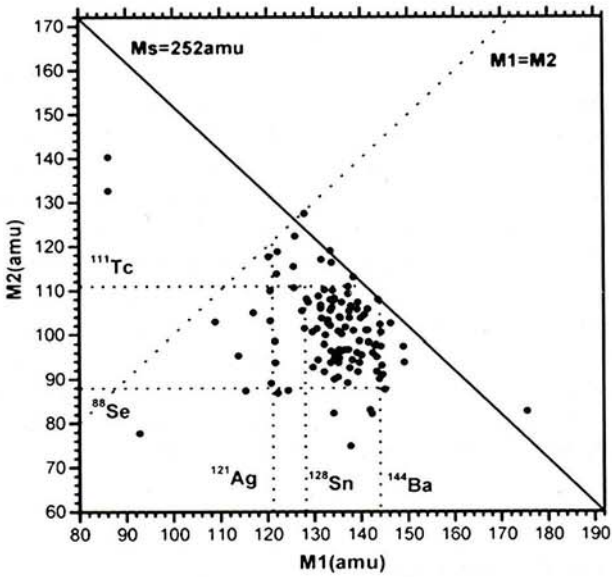

Fig. 6.44 Mass correlation plot for two heaviest partners of the multi-body decay of ^{252}Cf (*sf*)

The basic properties of the events joined, for instance, into *w*3-group are presented in Fig. 6.43(a) where $V_1 \sim V_{H\_bin}$ while $V_3 < V_2$. In order to reproduce the experimental velocity correlations the first rupture is supposed to occur between heavy Cs nucleus and di-nuclear system of Ni/P. After full acceleration this system decays making free both its constituents. The interaction energy E_{int} between the nuclei in the chain ^{70}Ni/^{39}P/^{143}Cs (taking into account both Coulomb and nuclear components), which converts into the total kinetic energy after scission, exceeds Q_3-value (Fig. 6.43(a)). An assumption of the decay via a more elongated quaternary configuration shown in Fig. 6.43(b) overcomes this difficulty.

Thus, the quaternary decay channel is predicted in the frame of the proposed scenario. Another indication of possible realization of quaternary collinear decay we see likely in our data from the COMETA setup where three fragments were

actually detected. Corresponding mass correlation plot m_1–m_2 is shown in Fig. 6.44. It shows clear rectangular structure bounded by the magic clusters. It should be stressed that for the bulk of events the total mass of three detected fragments is essentially less than the mass of the mother nucleus.

We are planning to develop different methodical approaches in order to perform cinematically complete experiment i.e. the direct registration of all (three and more) decay partners. Development of the COMETA setup is in progress. Additional mosaics of PIN-diodes will let to increase essentially the aperture and granularity of the spectrometer.

Digital image of the current impulses from the two CCT partners hit the same PIN-diode during registration gate can be obtained using fast flash-ADC ("double-hit" technique). Both energy and time-reference linked with each impulse will be calculated event by event.

Acknowledgements This text presents research results of the work supported in part by the grant of the Department of Science and Technology of South Africa and by a grant of the Federal Ministry of Education and Research (BMBF) of Germany. We would like to thank Prof. W. von Oertzen and Dr. W. Trzaska for fruitful collaboration.

Appendix

A.1 Reliability of Linear Structures in the Scatter Plot of Fragments Masses

Due to the small number of events in the linear structures discussed in Figs. 6.24(a), 6.26, 6.27, 6.29, 6.30 the question arises whether the structures have a physical reality, i.e. if they are not a random sequence of points. In order to answer this question a special simulation based on Hough transformation was performed.

The Hough transform is a feature extraction technique used in image analysis, computer vision, and digital image processing [74, 75]. The simplest case of Hough transform is the linear transform for detecting straight lines. In the image space, the straight line can be described as $y = mx + b$ and can be graphically plotted for each pair of image points (x, y). In the Hough transform, a main idea is to consider the characteristics of the straight line not as image points x or y, but in terms of its parameters, here the slope parameter m and the intercept parameter b. For computational reasons, it is better to parametrise the lines in the Hough transform with two other parameters, commonly referred to as R and θ (Fig. 6.45).

Actually, the straight line on a plane (Fig. 6.45) can be set as follows:

$$x \times \cos(\theta) + y \times \sin(\theta) = R, \tag{6.5}$$

where R—the length of the perpendicular lowered on a straight line from the beginning of coordinates, θ—angle between a perpendicular to a straight line and the axis OX, changes within the limits of 0–2π, R is limited by the size of the entrance image.

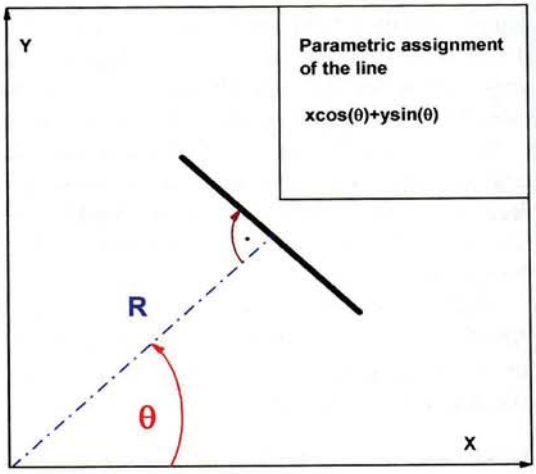

Fig. 6.45 Parameterization of the line in Hough transform

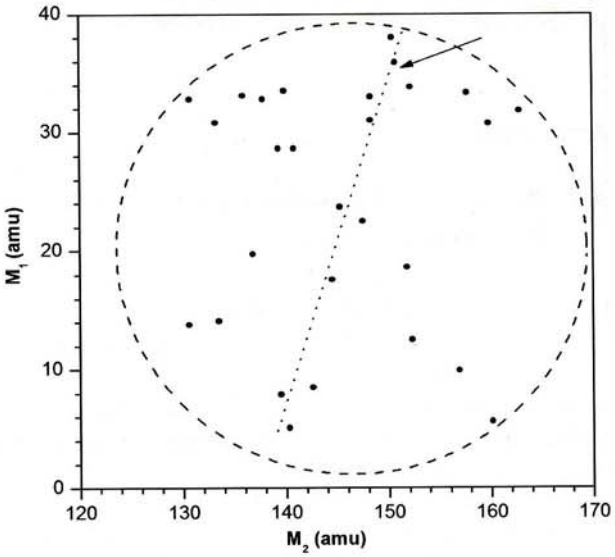

Fig. 6.46 Part of the distribution shown in Fig. 6.26(a) chosen for estimation of a reliability of the line structures. Monte-Carlo simulation were performed in the circle region marked by the *dash line*. See text for details

In view of step-type representation of entrance data (in the form of a matrix with elements "1"—presence of a point, "0"—it absence), the phase space (R, θ) also is represented in a discrete kind. In this space the grid to which one bin corresponds a set of straight lines with close values of R and θ is entered. For each cell of a grid $(R_i, R_{i+1}) \times (\theta_i, \theta_{i+1})$ (in other words for each Hough transform bin) the number of points with coordinates (x, y), satisfying to the equation (6.5), where $\theta_i \leq \theta \leq \theta_{i+1}$, $R_i \leq R \leq R_{i+1}$, is counted up. The size of bins is obtained empirically.

Besides the steps on R and θ $(\Delta R, \Delta\theta)$ in the real program code realizing Hough transform, there are the additional parameters responsible for the decision—whether all the points, satisfying Eq. (6.5), are necessary to attribute an analyzed straight line.

So, if the distance in pixels (cells of the matrix under analysis) between extreme points of a line segment less than set number n—it is rejected. When the code finds two line segments associated with the same Hough transform bin that are separated by less than the set distance d, it merges them into a single line segment.

A lower part of the scatter plot shown in Fig. 6.27 below $M_1 = 40$ amu was chosen for the analysis (Fig. 6.46). The straight line (marked by the arrow) united nine points was recognized using Hough transform algorithm at appropriate choice of the principal parameters (ΔR, $\Delta\theta$, n, d).

We tried to estimate the probability of a random realization of the line of such length and tilted to the abscissa axis at an arbitrary angle. A sequence of patterns within randomly distributed points inside was generated. Each circular pattern included precisely the same number of points as those in the initial distribution in Fig. 6.46. An area of circular shape was chosen in order to avoid a priori distinguished direction (for instance, diagonal in a rectangular area). Each pattern was processed with the Hough transform algorithm "tuned" earlier on revealing the line under discussion. Among one hundred patterns analyzed only two of them provided a positive answer. In other words, a probability of a random realization of the line under discussion is about 2 %.

Another approach based on the methods of morphological analysis of images [106, 107] was applied as well in order to estimate the probability of random realization of the rectangle seen in Fig. 6.26(b). This probability was estimated to be less than 1 %.

References

1. O. Hahn, F. Strassmann, Naturwissenschaften **27**, 89 (1939)
2. K.A. Petrzhak, G.N. Flerov, J. Phys. USSR **3**, 275 (1940)
3. L. Meitner, O. Frisch, Nature **143**, 239 (1939)
4. C.F. von Weizsäcker, Z. Phys. **96**, 431 (1935)
5. W.J. Swiatecki, in *Proceedings of the Second UN Conference on the Peaceful Uses of Atomic Energy*, Geneva, vol. 15 (United Nations, Geneva, 1958), p. 651
6. P. Möller, J.R. Nix, Nucl. Phys. A **272**, 502 (1976)
7. V.M. Strutinsky, N.Ya. Lyashchenko, N.A. Popov, Nucl. Phys. **46**, 639 (1963)
8. H. Diehl, W. Greiner, Phys. Lett. B **45**, 35 (1973)
9. H. Diehl, W. Greiner, Nucl. Phys. A **229**, 29 (1974)
10. G. Royer, J. Mignen, J. Phys. G, Nucl. Part. Phys. **18**, 1781 (1992)
11. X.-z. Wu, J.A. Maruhn, W. Greiner, J. Phys. G, Nucl. Part. Phys. **10**, 645 (1984)
12. D.N. Poenaru, W. Greiner, J.H. Hamilton, A.V. Ramayya, E. Hourany, R.A. Gherghescu, Phys. Rev. C **59**, 3457 (1999)
13. R.B. Tashkhodjaev, A.K. Nasirov, W. Scheid, Eur. Phys. J. A **47**, 136 (2011)
14. K. Manimaran, M. Balasubramaniam, Phys. Rev. C **83**, 034609 (2011)
15. K. Manimaran, M. Balasubramaniam, Eur. Phys. J. A **45**, 293 (2010)
16. V.I. Zagrebaev, A.V. Karpov, W. Greiner, Phys. Rev. C **81**, 044608 (2010)
17. K.R. Vijayaraghavan, W. von Oertzen, M. Balasubramaniam, Eur. Phys. J. A **48**, 27 (2012)
18. M.L. Muga, Phys. Rev. Lett. **11**, 129 (1963)
19. P. Schall, P. Heeg, M. Mutterer, J.P. Theobald, Phys. Lett. B **191**, 339 (1987)
20. F. Gönnenwein, Nucl. Phys. A **734**, 213 (2004)

21. P. Singer, Yu. Kopach, M. Mutterer, M. Klemens, A. Hotzel, D. Schwalm, P. Thirolf, M. Hesse, in *Proceedings of the 3rd International Conference on Dynamical Aspects of Nuclear Fission* (JINR, Dubna, 1996), p. 262
22. A.V. Ramayya et al., Phys. Rev. Lett. **81**, 947 (1998)
23. A.V. Ramayya et al., Prog. Part. Nucl. Phys. **46**, 221 (2001)
24. A.V. Daniel et al., in *Proceedings of the International Workshop on the New Applications of Nuclear Fission*, Bucharest, Romania (World Scientific, Singapore, 2004), p. 41
25. S.A. Karamian, I.V. Kuznetsov, Yu.Ts. Oganessian, Yu.E. Penionzhkevich, Yad. Fiz. **5**, 959 (1967)
26. P. Glässel, D.v. Harrach, H.J. Specht, L. Grodzins, Z. Phys. A **310**, 189 (1983)
27. C.-M. Herbach et al., Nucl. Phys. A **712**, 207 (2002)
28. G. Royer, F. Haddad, J. Phys. G, Nucl. Part. Phys. **20**, L131 (1994)
29. A.A. Ogloblin, G.A. Pik-Pichak, S.P. Tretyakova, in *Proceedings of the International Workshop Fission Dynamics of Atomic Clusters and Nuclei*, Luso, Portugal, 2000 (World Scientific, Singapore, 2001), p. 143
30. C. Wagemans, in *The Nuclear Fission Process*, ed. by C. Wagemans (CRS, Boca Raton, 1991). Chap. 12
31. E. Piasecki, M. Sowinski, L. Nowicki, A. Kordyasz, E. Cieślak, W. Czarnacki, Nucl. Phys. A **255**, 387 (1975)
32. S.W. Cosper, J. Cerny, R.C. Gatti, Phys. Rev. **154**, 1193 (1967)
33. Yu.V. Pyatkov, V.V. Pashkevich, Yu.E. Penionzhkevich, V.G. Tishchenko, C.-M. Herbach, in *Proceedings of the International Conference of Nuclear Physics "Nuclear Shells—50 Years"*, Dubna, 1999, ed. by Yu.Ts. Oganessian et al. (World Scientific, Singapore, 2000), p. 144
34. Yu.V. Pyatkov et al., in *Proceeding of the International Symposium on Exotic Nuclei EXON-2001*, Baikal Lake, 2001, ed. by Yu.E. Penionzhkevich et al. (World Scientific, Singapore, 2002), p. 181
35. H.-G. Ortlepp et al., Nucl. Instrum. Methods Phys. Res., Sect. A, Accel. Spectrom. Detect. Assoc. Equip. **403**, 65 (1998)
36. D.V. Kamanin et al., JINR Preprint 15-2007-182, Dubna (2007)
37. A. Oed, P. Geltenbort, F. Gönnenwein, Nucl. Instrum. Methods **205**, 451 (1983)
38. A.N. Tyukavkin et al., Instrum. Exp. Tech. **52**, 508 (2009)
39. Yu.V. Pyatkov et al., JINR Preprint E15-2004-65, Dubna (2004)
40. V.F. Apalin, Yu.N. Gritsyuk, I.E. Kutikov, V.I. Lebedev, L.A. Mikaelian, Nucl. Phys. **71**, 553 (1965)
41. L. Meyer, Phys. Status Solidi B **44**, 253 (1971)
42. A.V. Kravtsov, G.E. Solyakin, Phys. Rev. C **60**, 017601 (1999)
43. M.A. Mariscotti, Nucl. Instrum. Methods **50**, 309 (1967)
44. Yu.V. Pyatkov, V.G. Tishchenko, V.V. Pashkevich, V.A. Maslov, D.V. Kamanin, I.V. Kljuev, W.H. Trzaska, Nucl. Instrum. Methods Phys. Res., Sect. A, Accel. Spectrom. Detect. Assoc. Equip. **488**, 381 (2002)
45. B.D. Wilkins, E.P. Steinberg, R.R. Chasman, Phys. Rev. C **14**, 1832 (1976)
46. D. Rochman, I. Tsekhanovich, F. Gönnenwein, V. Sokolov, F. Storrer, G. Simpson, O. Serot, Nucl. Phys. A **735**, 3 (2004)
47. Yu.V. Pyatkov et al., Phys. At. Nucl. **73**, 1309 (2010)
48. D.V. Kamanin, Yu.V. Pyatkov, A.N. Tyukavkin, Yu.N. Kopatch, Int. J. Mod. Phys. E **17**, 2250 (2008)
49. Yu.V. Pyatkov et al., Rom. Rep. Phys. **59**, 569 (2007)
50. A.N. Tyukavkin et al., Preprint No. R15-2008-88, JINR (Joint Inst. Nucl. Res., Dubna, 2008)
51. Yu.V. Pyatkov et al., Eur. Phys. J. A **45**, 29 (2010)
52. D.V. Kamanin et al., in *Proceedings of the 18th International Seminar on Interaction of Neutrons with Nuclei: "Neutron Spectroscopy, Nuclear Structure, Related Topics"*, Dubna, 2010 (2011), p. 102
53. A.N. Tyukavkin et al., Prib. Teh. Eksp. **4**, 66 (2009)

54. A.A. Alexandrov et al., in *Proceedings of 15th International Seminar on Interaction of Neutrons with Nuclei: "Neutron Spectroscopy, Nuclear Structure, Related Topics"*, Dubna, 2007 (2008), p. 248
55. H. Märton, private communication
56. S.I. Mulgin, K.-H. Schmidt, A. Grewe, S.V. Zhdanov, Nucl. Phys. A **640**, 375 (1998)
57. V.V. Pashkevich, Yu.V. Pyatkov, A.V. Unzhakova, Int. J. Mod. Phys. E **18**, 907 (2009)
58. Yu.V. Pyatkov et al., Eur. Phys. J. A **48**, 94 (2012)
59. C. Butz-Jorgensen, H.H. Knitter, Nucl. Phys. **490**, 307 (1988), and Refs. therein
60. D.V. Kamanin et al., Phys. At. Nucl. **66**, 1655 (2003)
61. S.I. Mulgin, V.N. Okolovich, S.V. Zhdanov, Nucl. Instrum. Methods Phys. Res., Sect. A, Accel. Spectrom. Detect. Assoc. Equip. **388**, 254 (1997), and Refs. therein
62. M. Moszyński, B. Bengtson, Nucl. Instrum. Methods **91**, 73 (1971)
63. Yu.V. Pyatkov et al., in *Proceedings of the 14th International Seminar on Interaction of Neutrons with Nuclei: "Neutron Spectroscopy, Nuclear Structure, Related Topics"*, Dubna, 2006 (2007), p. 134
64. D.V. Kamanin et al., in *Proceedings of the International Symposium on Exotic Nuclei (EXON-2009)*, ed. by Yu.E. Penionzhkevich et al. AIP Conference Proceedings, Sochi, 2009, p. 385
65. J.F. Wild et al., Phys. Rev. C **41**, 640 (1990)
66. O. Sorlin et al., Phys. Rev. Lett. **88**, 092501 (2002)
67. V.K. Rao, V.K. Bhargava, S.G. Marathe, S.M. Sahakundu, R.H. Iyer, Phys. Rev. C **9**, 1506 (1974)
68. V.K. Rao, V.K. Bhargava, S.G. Marathe, S.M. Sahakundu, R.H. Iyer, Phys. Rev. C **19**, 1372 (1979)
69. C. Wagemans (ed.), *The Nuclear Fission Process* (CRC Press, Boca Raton, 1991). Chap. 6
70. F. Gönnenwein, M. Mutterer, Yu. Kopatch, Europhys. News **36**, 11 (2005)
71. A.N. Tyukavkin, PhD thesis, MEPhI, Moscow (2009)
72. MCNP—Monte Carlo N-Particle code. http://mcnp-green.lanl.gov
73. B.D. Wilkins, E.P. Steinberg, R.R. Chasman, Phys. Rev. C **14**, 1832 (1976)
74. http://en.wikipedia.org/wiki/Hough_transform
75. L.G. Shapiro, G.G. Stockman, *Computer Vision* (Prentice Hall, New York, 2001)
76. N.V. Kornilov, F.-J. Hambsch, A.S. Vorobyev, Nucl. Phys. A **789**, 55 (2007)
77. A.S. Vorobyev, O.A. Shcherbakov, Yu.S. Pleva, A.M. Gagarski, G.V. Val'ski, G.A. Petrov, V.I. Petrova, T.A. Zavarukhina, in *Proceedings of the 17th International Seminar on Interaction of Neutrons with Nuclei: "Neutron Spectroscopy, Nuclear Structure, Related Topics"*, Dubna, 2009 (2010), p. 60
78. www.srim.org
79. U. Quade et al., Nucl. Phys. A **487**, 1 (1988)
80. H. Wohlfarth, W. Lang, H. Dann, H.-G. Clerc, K.H. Schmidt, H. Schrader, Z. Phys. A **287**, 153 (1978)
81. FZR 92-09, Mai 1992, Herausgeber: H. Prade, F. Donau.
82. D.V. Kamanin et al., in *Proceedings of the 7th International Conference on Dynamical Aspects of Nuclear Fission (DANF-2011)*, Smolenice Castle (2011 in press)
83. Y.S. Kim, P. Hofmann, H. Daniel, T. von Egidy, T. Haninger, F.-J. Hartmann, M.S. Lotfranaei, H.S. Plendl, Nucl. Instrum. Methods Phys. Res., Sect. A, Accel. Spectrom. Detect. Assoc. Equip. **329**, 403 (1993)
84. D. Poenaru, W. Greiner, in *Cluster in Nuclei, vol. 1*, ed. by C. Beck. Lect. Notes Phys., vol. 818 (2010), p. 1
85. V. Zagrebaev, W. Greiner, in *Cluster in Nuclei, vol. 1*, ed. by C. Beck. Lect. Notes Phys., vol. 818 (2010), p. 267
86. G.G. Adamian, N.V. Antonenko, W. Scheid, in *Cluster in Nuclei, vol. 2*, ed. by C. Beck. Lect. Notes Phys., vol. 848 (2012), p. 165
87. D.V. Kamanin et al., in *Proceedings of the 18th International Seminar on Interaction of Neutrons with Nuclei: "Neutron Spectroscopy, Nuclear Structure, Related Topics"*, Dubna,

2010 (2011), p. 102
88. F. Gönnenwein, M. Mutterer, A. Gagarski, I. Guseva, G. Petrov, V. Sokolov, T. Zavarukhina, Yu. Gusev, J. von Kalben, V. Nesvizhevski, T. Soldner, Phys. Lett. B **652**, 13 (2007)
89. Yu. Pyatkov et al., in *Proc. of the Int. Symposium on Exotic Nuclei "EXON2006"*. AIP Conference Proceedings, Khanty-Mansiysk, Russia, 2006 (2007), p. 144
90. Yu. Pyatkov et al., in *Proc. 14th Int. Sem. on Interaction of Neutrons with Nuclei "ISINN-14"* (JINR, Dubna, 2007), p. 134
91. Yu. Pyatkov (HENDES and FOBOS Collaborations), *Proc. VI Int. Conf. on Dynamical Aspects of Nuclear Fission "DANF2006"* (World Scientific, Singapore, 2008), p. 248
92. Yu. Pyatkov (HENDES and FOBOS Collaborations), *Proc. 15th Int. Sem. on Interaction of Neutrons with Nuclei "ISINN-15"* (JINR, Dubna, 2008), p. 281
93. D.V. Kamanin et al., Phys. Part. Nucl. Lett. **7**, 122 (2010)
94. S.H. Freid, J.L. Anderson, G.R. Choppin, J. Inorg. Nucl. Chem. **30**, 3155 (1968)
95. M.L. Muga, C.R. Rice, W.A. Sedlacek, Phys. Rev. Lett. **18**, 404 (1967)
96. Yu.V. Pyatkov, G.G. Adamian, N.V. Antonenko, V.G. Tishchenko, Nucl. Phys. A **611**, 355 (1996)
97. Yu.V. Pyatkov, V.V. Pashkevich, Yu.E. Penionzhkevich, V.G. Tishchenko, A.V. Unzhakova, H.-G. Ortlepp, P. Gippner, C.-M. Herbach, W. Wagner, Nucl. Phys. A **624**, 140 (1997)
98. I. Tsekhanovich, H.-O. Denschlag, M. Davi, Z. Buyukmumcu, F. Gonnenwein, S. Oberstedt, H.R. Faust, Nucl. Phys. A **688**, 633 (2001)
99. Yu.V. Pyatkov, V.V. Pashkevich, W.H. Trzaska, G.G. Adamian, N.V. Antonenko, D.V. Kamanin, V.A. Maslov, V.G. Tishchenko, A.V. Unzhakova, Phys. At. Nucl. **67**, 1726 (2004)
100. V.V. Vladimirski, JETP USSR **5**, 673 (1957)
101. Yu.V. Pyatkov, R.A. Shekhmametiev, Phys. At. Nucl. **57**, 1182 (1994)
102. S. Ćwiok, W. Nazarewicz, J.X. Saladin, W. Płóciennik, A. Johnson, Phys. Lett. B **322**, 304 (1994)
103. D.M. Gorodisskiy, S.I. Mulgin, V.N. Okolovich, A.Ya. Rusanov, S.V. Zhdanov, Phys. Lett. B **548**, 45 (2002)
104. V.V. Pashkevich, Nucl. Phys. A **169**, 275 (1971)
105. Yu.V. Pyatkov, D.V. Kamanin, W. von Oertzen, A.A. Alexandrov, I.A. Alexandrova, N.A. Kondtayev, E.A. Kuznetsova, O.V. Strekalovsky, V.E. Zhuchko, in *Proc. 20 International Seminar on Interaction of Neutrons with Nuclei "ISINN-20"*, Alushta, Ukraine (JINR, Dubna, 2013), p. 104
106. Yu.P. Pytyev, Pattern Recognit. Image Anal. **3**, 19 (1993)
107. Yu.V. Pyatkov, D.V. Kamanin, O.V. Falomkina, Yu.P. Pyt'ev, B.M. Herbst, W.H. Trzaska, Pattern Recognit. Image Anal. **20**, 82 (2011)